Thermodynamic properties, interfacial adhesion energy and tribological properties between MCN (M = Hf, Ta, Cr, Nb) coating and Ti alloy substrates investigated by experiment and first-principles calculations

Mengjuan Yin [a], Wenping Liang [a], Qiang Miao [a e], Haiyang Yu [a], Yuehao Xu [a], Jiumei Gao [a], Shijie Sun [b], Hongmei Jin [c], Daniel.J Blackwood [d]

[a] College of Materials Science and Technology, Nanjing University of Aeronautics and Astronautics, Nanjing 211106, China

[b] National Key Laboratory of Advanced Composites, AECC Beijing Institute of Aeronautical Materials, Beijing 100095, China

[c] Institute of High-Performance Computing, Agency for Science, Technology and Research, 1 Fusionopolis Way, #16-16 Connexis, Singapore 138632, Singapore

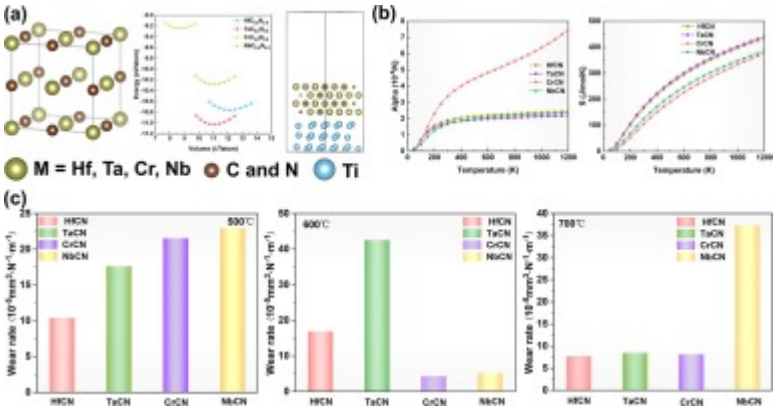
[d] Department of Materials Science & Engineering, National University of Singapore, 9 Engineering Drive 1, Singapore 117575, Singapore

[e] Wuxi Research Institute, Nanjing University of Aeronautics and Astronautics, China

Abstract

A series of MCN (M = Hf, Ta, Cr, Nb) coatings were prepared by double glow plasma surface alloying (DGPSA) as protective hard coatings for Ti60 (Ti-5.5Al-4.0Zr-4.0Sn), aiming to solve the problems of low bonding strength between the ceramic coating and the substrate as well as the poor wear resistant of ceramic alloy coatings. First principles calculation was used to study the elastic constant of $MC_{0.5}N_{0.5}$ solids, thermomechanical parameters and the interfacial adhesive strength of Ti(1 0 1)/MCN(2 2 0). The calculated results indicated the HfCN solids show excellent mechanical properties, lower thermal expansion coefficient α, lower Gibbbs values and higher values of entropy (S), superior adhesion strength $W_{ad} \sim 5.7$ J/m^2. The high-temperature tribological performance tests show that the HfCN and TaCN coatings exhibited better wear resistance compared with the CrCN and NbCN coatings at 500 °C -700 °C. The wear rate of HfCN coatings at 500 °C and 700 °C is about 2 times and 5 times lower than that of CrCN, which is in accordance with the HfCN coating's excellent thermal stability and high interfacial bonding strength with the Ti substrate. The adhesion wear mechanism of all coatings gradually intensified with increasing temperature.

Graphical abstract



Keywords
Double glow plasma surface alloying
MCN coatings
First principles calculation
Thermal stability
Interfacial adhesion strength
High temperature tribological performance

1. Introduction

Titanium and its alloy with high strength-to weight ratio, excellent creep resistance and thermal fatigue property, are promising critical materials for high-temperature components, such as rocket thrust chambers, high-temperature superconducting trains and engine combustion chambers. However, their applications are severely restricted owing to the wear and friction between counterparts and Ti-alloy easily occurs at around 500 °C–700 °C [1]. To overcome the disadvantages, alloying high-temperature protection methods are generally applied such as protection coatings and grain refinement [2], [3], [4]. Among them, the alloying method of adding metallic (Cr, Hf, Ta, et al) and/or non-metallic elements to the Ti matrix can improve the high-temperature oxidation and wear resistance, but the mechanical properties commonly degrade [5]. The grain refinement methods, including shot/laser peening [6], [7], [8], can only enhance the wear resistance to a limited extent. However, a high strength and high toughness coating could essentially solve the damage of the coating to the substrate. The transition-metal (TM) carbonitrides (TMCN, M = 3d, 4d or 5d TM) with a B1-NaCl structure have become promising candidates due to the combined advantages and features of both transition-metal carbides (TMC) and transition-metal nitrides (TMN) [9], [10], meanwhile present higher hardness [11], excellent wear resistance [12], [13], thermal stability [14] and form a self-adaptive friction-induced glaze layer during friction conditions [15].

Traditionally, the performance of a coating can be affected by numerous factors including its hardness (H), elastic modulus (E), H/E ratio and its adhesion to the matrix [15], [16]. Generally, the adhesion is determined by the microstructure at the interface, as well as the strength of atomic bonds between the matrix and the coating [17]. The double glow plasma surface alloy (DGPSA) can obtain excellent metallurgical bonding between the coatings and the matrix, dense microstructure and adjustable thickness of the coatings. Based on these advantages, DGPSA has been applied to improve high-temperature wear resistance of Ti alloy via preparing different coatings, such as CrN, ZrTaN, (ZrTaNb)C/N and plasma nitriding coatings [18], [19], [20], [21]. Nevertheless, there are still some problems to be solved, such as high cracking sensibility and large difference in the thermal expansion coefficients between the ceramic coating and the matrix. It is challenging to assess the binding

properties through experimental methods due to the extremely thin layers of TMCN coating on the surface of Ti alloy. Meanwhile, it is necessary to select suitable ternary TMCN coating to mitigate the friction conditions during application, such as the refractory TM elements: Cr, Hf, Nb, Ta, with thermal stability and superior mechanical properties [13], [15], [22], [23].

First-principles calculations are widely used in modern scientific research owing to the fact they can reveal the interface structures at atomic and electronic levels. It is a valuable tool for a thorough explanation of interface problems, such as the stability of interfaces [24]. Many investigations have demonstrated the significance of theoretical computation in the study of interface structures [24], [25]. The lack of atomic resolution in traditional experiments can be compensated for by this method. Moreover, the first-principles method can be used to calculate the thermodynamic parameters systematically [26], [27], e.g. entropy, thermal expansion coefficient, heat capacity and so on, which make it possible to find a proper method to overcome the difficulty of obtaining the thermodynamic data during the experiments and applications.

In this work, the MCN coatings with different transitional metal M = Hf, Ta, Cr, Nb were prepared through sputtering a MC target by changing the M type in the target, with an atmosphere of a mixture Ar and N_2 gases. The indentation test was used to evaluate the mechanical properties of MCN coatings combined with the theoretical calculation. The scratch test of MCN coatings was applied to evaluate the bonding strength between the coating and the substrate. For comparison, the adhesion and interfacial energy of Ti (1 0 1)/MCN (2 2 0) interface were calculated by first-principles method. Moreover, the tribological property of the MCN coatings at 500 °C ~700 °C was studied, with an in-depth analysis of the wear mechanism at high temperatures based on the calculated thermodynamic parameters of $MC_{0.5}N_{0.5}$. The results will provide an invaluable resource for further theoretical and experimental research.

2. Methods

2.1. Materials and experimental procedures

The investigations were performed on workpieces made of the high-temperature titanium alloy Ti-5.5Al-4.0Zr-4.0Sn, also known as Ti60, with the size of 10 × 10 × 5 mm^3. Prior to the experiments, the workpieces were ground with 180#-2000# sandpaper, followed by polishing with Cr_2O_3 suspension to mirror and cleaning with ultrasonic for 15 min in ethanol. Before sputtering, the Ar ion bombardments were performed for 15 min with 400 V of the specimen cathode voltage and 600 V of the source electrode voltage to eliminate the contamination on the surfaces of target. The pressure in vacuum chamber was maintained at 35 Pa. Subsequently, the MCN coatings were deposited by sputtering the source electrode targets composed by the pure M (M=Hf, Ta, Cr, Nb) and C plates (≧ 99.95 %) with a size of 60 × 20 × 4 mm^3 of each plate, under a mixture gas of Ar (working gas) and N_2 (reaction gas). The flow rate of N_2 gas is 30 sccm. The detail sputtering parameters are listed in Table 1.

Table 1. Experimental parameters used for sputtering MCN coatings.

Parameters	**Values**	**Composition of targets**		**Ar/N_2 flow ratio**	**Target-substrate distance (mm)**
		MCN coatings	**Types of plate**		
Sputtering time (h)	4	HfCN	Hf and C plates	3:1	16 ~ 20
Sputtering pressure (Pa)	35	TaCN	Ta and C plates		
Source voltage (V)	800	CrCN	Cr and C plates		

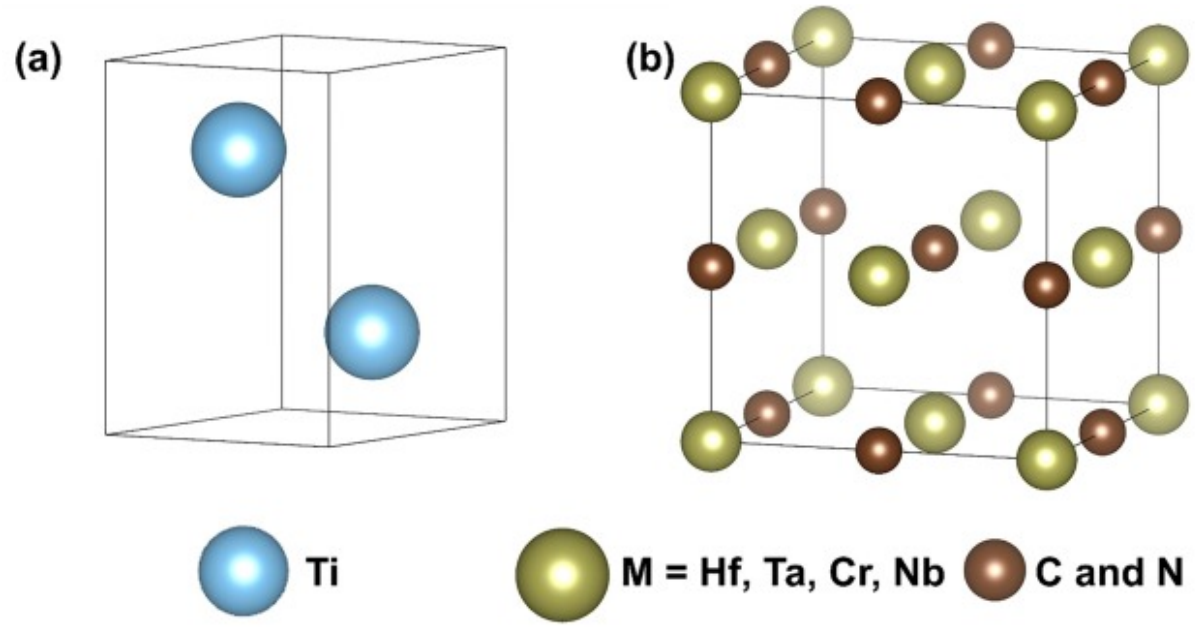
Parameters	Values	Composition of targets		Ar/N_2 flow ratio	Target-substrate distance (mm)
		MCN coatings	Types of plate		
Cathode voltage (V)	400	NbCN	Nb and C plates		

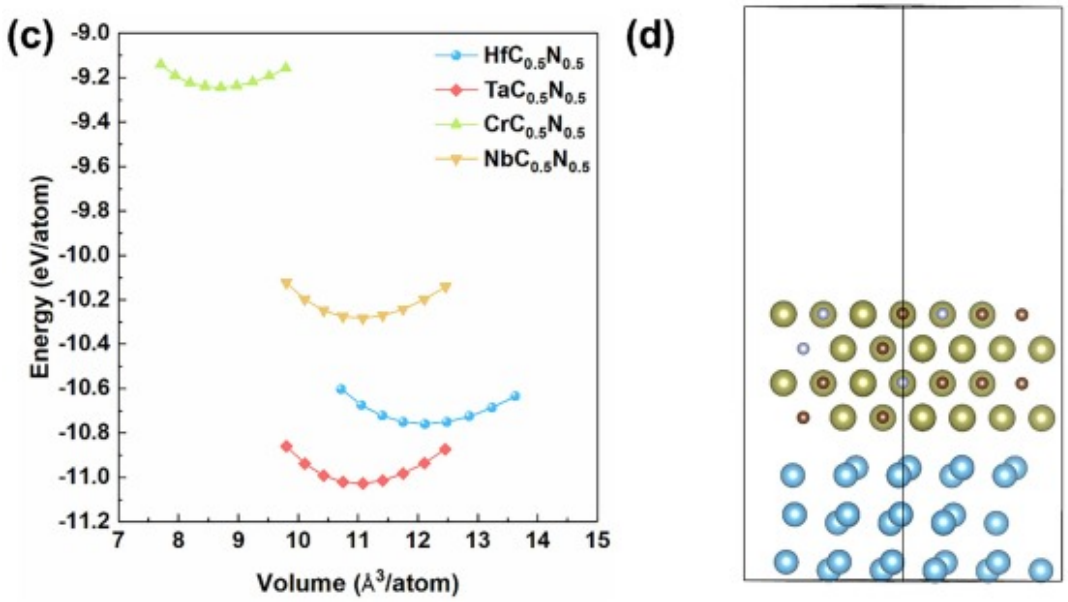
The surface and cross-sectional morphologies of the MCN coatings were investigated using a scanning electron microscope (SEM, Scios 2, Czech), the chemical component of the coatings was examined by an energy dispersive spectroscopy (EDS, Scios 2, Czech). The X-ray diffraction (XRD, PAN alytical, Holland) was used to characterize the phase compositions of the MCN coatings with Cu Kα radiation (λ = 1.54060 Å), at the 2θ range from 20° to 90°. The scratch tests were performed on the WS-2005 Coating Adhesion Automatic Scratch Tester (Lanzhou Kaihua) using a 120° diamond pyramid indenter. A progressive load (0 N to 80 N) at a loading rate of 80 N/min was applied to the indenter, and obtained a scratch length of 5 mm. Each sample scratch three times at different area on the coating surface. The images of the scratches were observed by SEM to identify the initial failure load (L_{c1}), partial exposure of the substrate (L_{c2}), and the crack propagation resistance (CPR) uses as a qualitative measurement of the coating's scratch toughness and longevity corresponding to the formula [28]:(1)V=Lh3h2+4b2/6b

The friction and wear tests of the MCN coatings were performed on the ball-on-disk tribometer (HT-1000, Lanzhou, China). The Si_3N_4 ball (2196 HV5) [29] with a diameter of 4 mm was used as the counterpart, the applied load (F) was 330 g, the rotational speed (v) was 560 r/min, and the sliding time (t) was 15 min. The three-dimension profile of the wear tracks were measured by the SMT-5000 device. The wear rate (W_r) of the MCN coatings at 500 °C, 600 °C and 700 °C were obtained from the following equation:(2)Wr=V/F·v·t(3)V=Lh3h2+4b2/6bThe wear volume (V) [21] can be calculated by the length (L), the depth (h) and width (b) of the wear tracks. The wear mechanism of the coatings was determined from the SEM images and EDS analysis of the wear tracks on the coatings and the wear tracks of the count body, as well as combined with the theoretical calculations of the thermodynamic properties of the $MC_{0.5}N_{0.5}$ crystals. X-ray photoelectron spectroscopy (XPS, Thermo Fisher K-Alpha+) using Ar^+ cleaning was applied to detect the wear and oxidation products on the wear surface. Prior to and following the measurements, the C1s core level signal was measured to calibrate the binding energy (BE) scale [19].

2.2. Computational details

The pure carbides and nitrides e.g. MC/N (M = Hf, Ta, Cr, Nb) crystallize in the Fm3m space group (2 2 5), and the Ti is a close-packed hexagonal structure with a P63/mmc space group (194, Fig. 1a). The lattice constants of related pure carbides and nitrides from previous studies are shown in Table 2. For convenience of comparison, the structure of carbonitrides MCN in this paper are simulated beginning with 32 transition metal atoms (M), 16 C atoms and 16 N atoms as shown in Fig. 1b. For $MC_{0.5}N_{0.5}$ systems, the total energy E as a function of volumes V are calculated during optimization. Fig. 1c shows the results of fitting the third-order Brich-Murnaghan equation of state (EOS). The optimized equilibrium lattice constants in this study are listed in Table 2, derived from the fitting E-V curves. The crystal structures of Ti and $MC_{0.5}N_{0.5}$ (Fig. 1d) are fully relaxed to guarantee the stability of the structure used in the calculation. The optimized lattice parameters demonstrate good accuracy when compared to other calculated and experimental values (Table 2).





1. Download: Download high-res image (361KB)
2. Download: Download full-size image

Fig. 1. The crystal structures of Ti (a), MCN (b), E-V curves for $MC_{0.5}N_{0.5}$ (M = Hf, Ta, Cr, Nb) with distortion (c) and interfacial model of Ti (1 0 1)/MCN (2 2 0) (d).

Table 2. Lattice constants a (Å) for $MC_{0.5}N_{0.5}$ carbonitrides (M = Hf, Ta, Cr, Nb), and the lattice constants on the related pure carbides and nitrides are provided for comparison.

Compounds	Calc. (this work)	Calc. (other data)	Exp.
$HfC_{0.5}N_{0.5}$	4.589	4.592[30], 4.676[10]	4.681[10]
HfN		4.537[30], 4.646[10]	4.65[10], 4.54[30]
$TaC_{0.5}N_{0.5}$	4.435		
TaC		4.485[31], 4.566[32]	4.58[33], 4.564[34]

Compounds	Calc. (this work)	Calc. (other data)	Exp.
$CrC_{0.5}N_{0.5}$	4.095		
CrN		4.049[35], 4.047[36], 4.057[37]	4.148[38], 4.130[37]
$NbC_{0.5}N_{0.5}$	4.439		
NbC		4.44[30], 4.53[30]	4.48[33], 4.47[30]

To calculate the elastic constants of $MC_{0.5}N_{0.5}$ and the interface properties of $MC_{0.5}N_{0.5}$ and Ti. the DFT-based simulations were carried out with the Vienna Ab-initio Simulation Package (VASP) [39]. Model visualizations were generated using VESTA software [40]. The exchange–correlation energy was described using the generalized gradient approximation (GGA) functional of Perdew-Burke-Ernzerhof (PBE)[41], [42].

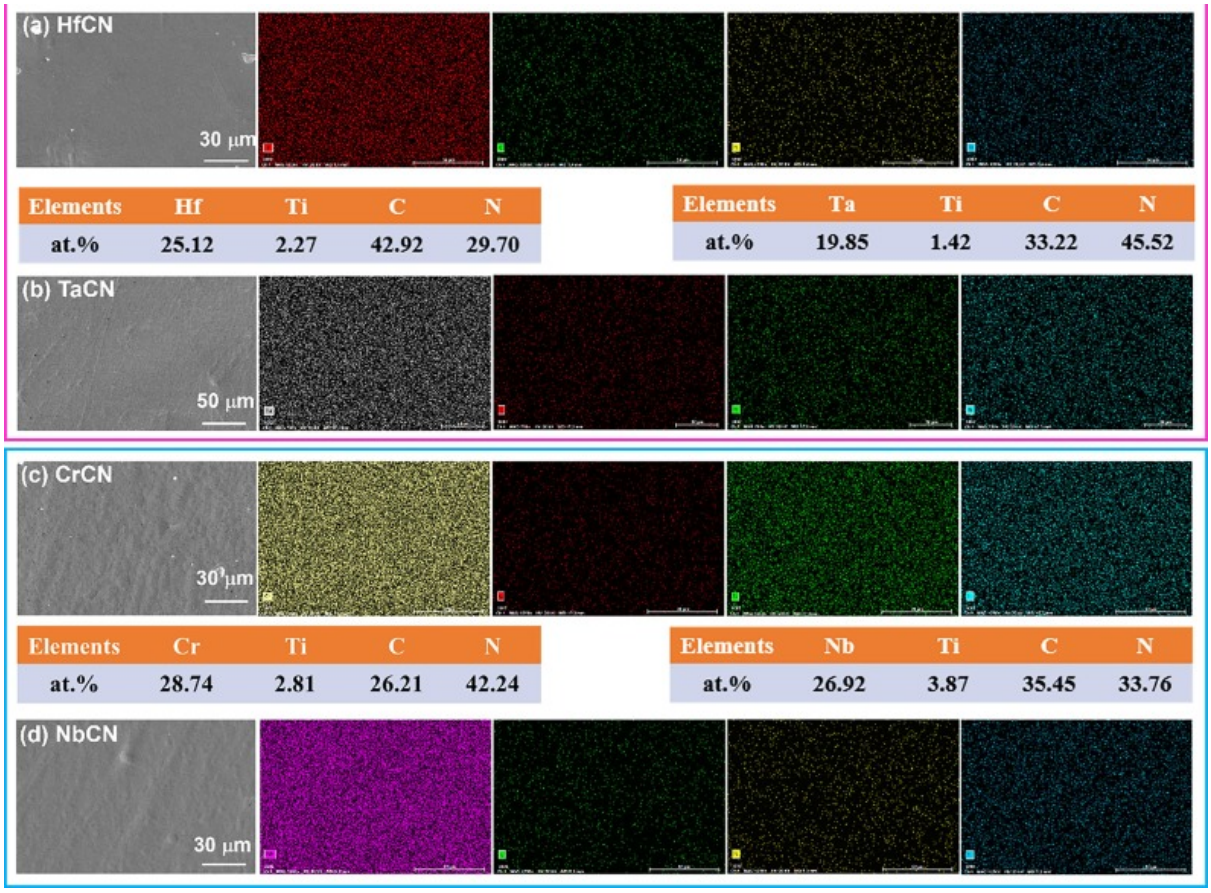
To ensure calculation accuracy, the atomic wave function energy cutoff (ENCUT) and convergence tests for K-points were performed. The Monkhorst-Pack method was used to determine the K-points, with an energy difference between successive steps set to be less than 0.015 eV/atom, serving as the ionic convergence standard. The ENCUT values for $MC_{0.5}N_{0.5}$, and interfacial model calculations were set at 520 eV. For Ti bulk, MCN bulk, and Ti/MCN interface calculations, the K-points were set to 3 × 2 × 1. The convergence criterion for the energy change was less than 1.0×10^{-5} eV/atom. To mitigate surface atom interactions, 15 Å vacuum layers were included in the surface and interface models, as shown in Fig. 1c. The adhesive strength of Ti (1 0 1)/MCN (2 2 0) were calculated, to more accurately simulate the real situation of the interface according to the preferred orientation plane of substrate and coating. Additionally, spin polarization was considered when considering the magnetic effects of Cr atoms.

Within the VASP code, the second-order elastic constants of the $MC_{0.5}N_{0.5}$ are determined using the energy-strain method. Then, the elastic constants C_{ij} was used to characterize the bulk modulus B, shear modulus G, Young's modulus E, and Poisson's ratio v. And the values of B, G, E and v are calculated by the following equations using the Voigt-Reuss-Hill approximations.(4)B=BV+BR2(5)G=GV+GR2(6)E=9BG3B+G(7)v=3B-2G2(3B+G)where the subscripts R and V stand for the Reuss and Voigt bounds, respectively.

The first-principles method combined with the quasi-harmonic Debye model performed by the GIBBS2 package [41], [43] was used for the study of the thermo-physical properties of the MCN. After that, from derivatives of Helmholtz free energy F as referred in reference [27], basic thermodynamic properties can be derived [44].

3. Results and discussion

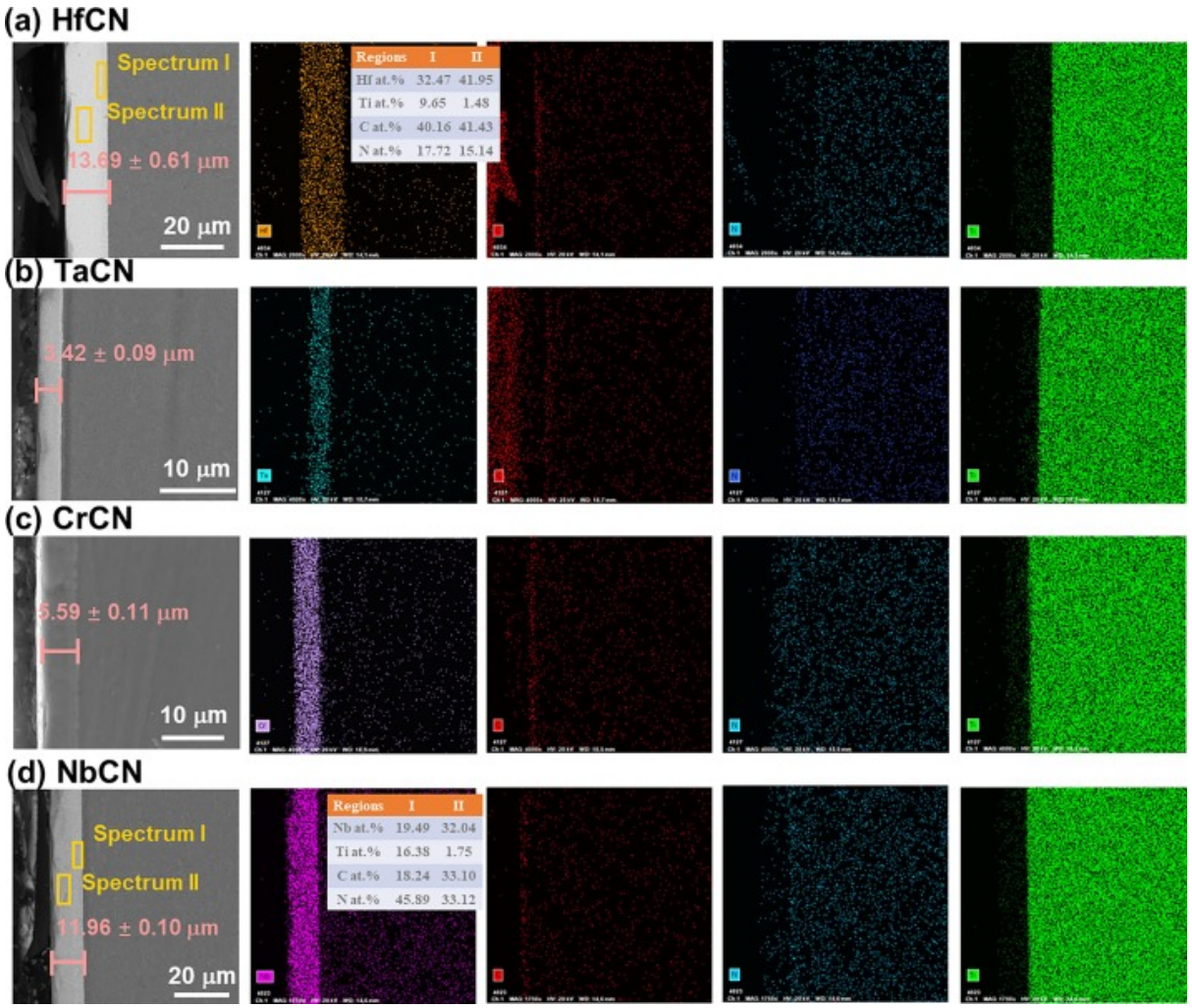
The surface morphology and chemical components of MCN coatings with different M types in the source electrode target by DGPSA are displayed in Fig. 2. The surfaces of all the samples exhibit few defects and are of high density, which are typical characteristics of DGPSA [45], [46]. This can be attributed to the deposition method of holding for a long time at high temperature, the M atoms are deposited with increasing ion bombardment, filling the defects between the scales. The EDS analysis indicates that the surface of MCN coatings mainly consists of M, C and N elements, and little Ti from the Ti60 substrate.



1. Download: Download high-res image (2MB)
2. Download: Download full-size image

Fig. 2. The SEM images and corresponding EDS surface scan of MCN coatings (M = Hf, Ta, Cr, Nb): HfCN (a), TaCN (b), CrCN (c), and NbCN (d).

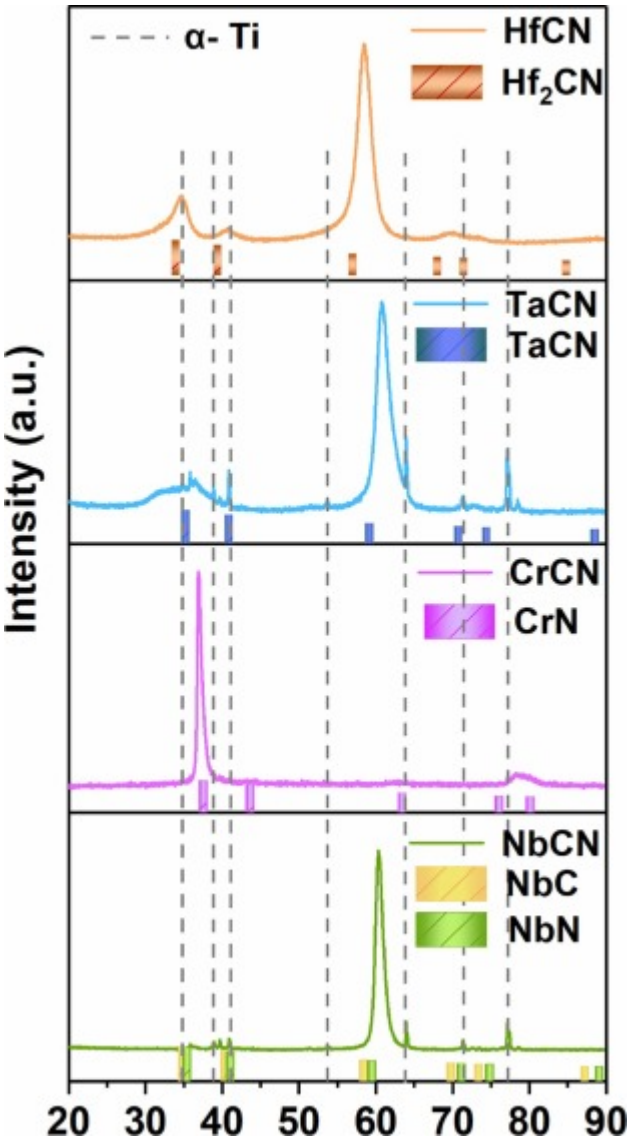
Fig. 3 displays the cross-sectional SEM morphologies and EDS points scan analysis of MCN coatings. Obviously, there are no pores and cracks among these cross-sectional samples. The coatings (including deposition and interdiffusion layer) and the substrates show good adhesion. The coating thickness varies greatly under the same holding time, which may be attributed to the differing sputtering rates and deposition rates of various M elements. For example, the TaCN and CrCN samples show relatively thin deposition layers, only ~3.42 μm and 5.59 μm, whereas for the Hf and Nb samples, the thickness increases to ~ 13.69 μm and 11.96 μm. The EDS results indicate that the dense alloy coatings can be attributed to the concentration gradient of MCN from the top surface of the coatings (Spectrum II) to the near substrate (Spectrum I). The elemental concentration of M, C and N shows a decreasing trend from the top surface to the substrate, while the Ti diffused from the substrate shows the opposite trend, which is consistent with the Ti detected on the surface in Fig. 2. Note that, the EDS analysis for M=Ta and Cr samples has been ignored owing to the thickness of the coatings being too thin. It is concluded that a metallurgical bonding occurs between the MCN coating and Ti60 substrate is produced by the interstitial diffusion of M and C/N ions/atoms, as well as the mutual diffusion of M and Ti between the deposited layer and Ti substrate.



1. Download: Download high-res image (1MB)
2. Download: Download full-size image

Fig. 3. The cross-sectional SEM images and corresponding EDS surface scan of MCN coatings (M = Hf, Ta, Cr, Nb): HfCN (a), TaCN (b), CrCN (c), and NbCN (d).

Fig. 4 shows the XRD analysis of MCN samples, all the samples have fcc solid solution phase, while the α-Ti phase (PDF#89-3725) was detected at the Ti-based coatings, which confirmed the occurrence of the interdiffusion of atoms in the coatings and the substrate during the deposition process. According to the PDF cards corresponding to the MCN coatings, it can be observed that the MCN coatings mainly consist of Hf_2CN phase (PDF#89-7440, HfCN sample), TaCN phase (PDF#89-3691, TaCN sample), CrN phase (PDF#77-0047, CrCN sample) and NbC, NbN phases (PDF#89-3830 and PDF#71-0162, NbCN sample). The dominant peaks of the HfCN, TaCN and NbCN samples are located at about $2\theta = 59°$, the reason for this can be attributed to the (2 2 0) preferred orientation of Hf, Ta, Nb atoms, while the primary diffraction peaks of CrCN sample is located at $\sim 2\theta = 37.5°$ (1 1 1). It can be observed that a noticeable broadening of the diffraction peak from 37° to 42° of MCN samples (M = Hf, Ta, Nb) compared to CrCN sample, suggesting that these coatings have smaller crystal sizes compared to CrCN sample [19], which corresponds to the SEM morphologies in Fig. 2.



1. Download: Download high-res image (239KB)
2. Download: Download full-size image

Fig. 4. The X-ray spectrum of MCN coatings (M = Hf, Ta, Cr, Nb).

The second-order elastic constants of MCN (M = Hf, Ta, Cr, Nb) solid solutions were calculated using energy-strain method as listed in Table 3. The mechanical stability of crystalline structures must satisfy the stability criteria. For cubic crystals, the mechanically stability criteria are $C_{11} > 0$, $C_{44} > 0$, $C_{11}-C_{12} > 0$, $C_{11} + C_{12} > 0$ [47]. Obviously, the calculated C_{ij} for $MC_{0.5}N_{0.5}$ solid solutions fulfill with the mechanically stability criteria. For comparison, the previous references of the calculated and experimental elastic constants are also shown in Table 3. The results of this study are in good agreement with the previous investigations. The bulk modulus of $TaC_{0.5}N_{0.5}$ is larger than $HfC_{0.5}N_{0.5}$ and $CrC_{0.5}N_{0.5}$, indicating that the former has greater ability to resist volume changes [10], [41], [48]. Notably, the shear modulus G (190.76 GPa) and Young's modulus E (458.57 GPa) of $HfC_{0.5}N_{0.5}$ and $TaC_{0.5}N_{0.5}$ are larger than the other two phases, implying that $HfC_{0.5}N_{0.5}$ and $TaC_{0.5}N_{0.5}$ have higher ability to withstand reversible deformations under shear stress and more stiffness than the other two solid solutions. The hardness of $MC_{0.5}N_{0.5}$ are predicted by well-established equations: $Hv = 2(G^3/B^2)^{0.585} - 3$ [27], among them, the $HfC_{0.5}N_{0.5}$ presents the highest

hardness. As for $CrC_{0.5}N_{0.5}$, although the H_v value is relatively high, the B, G and E values are the lowest among the four $MC_{0.5}N_{0.5}$ compositions.

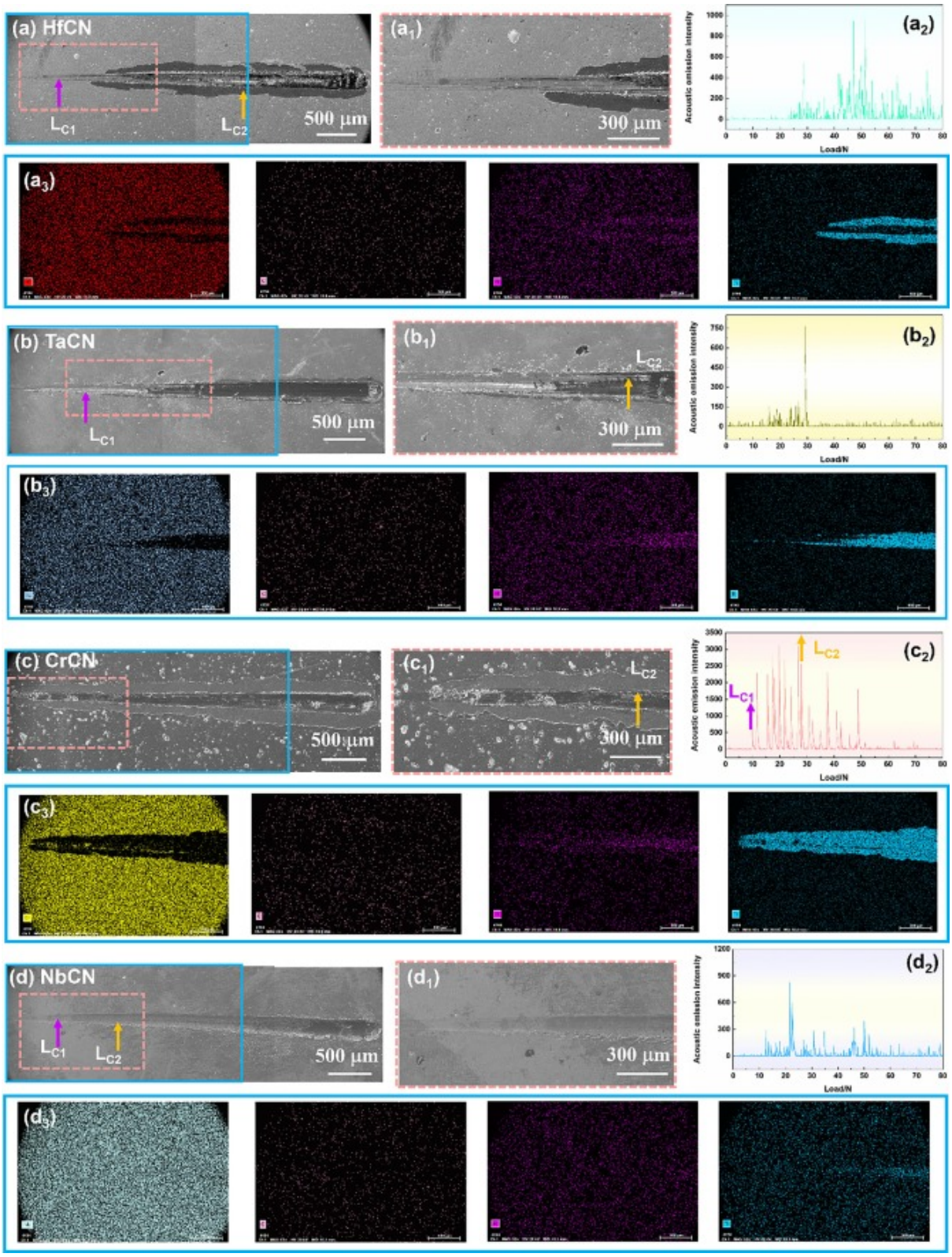
Table 3. The elastic constants C_{ij} (GPa), bulk modulus (GPa), shear modulus (GPa), Young's modulus (GPa), Poisson's ration v, Pugh's ratio (B/G) and Cauchy pressure of $MC_{0.5}N_{0.5}$ phases.

Empty Cell	**$HfC_{0.5}N_{0.5}$**	**$TaC_{0.5}N_{0.5}$**	**$CrC_{0.5}N_{0.5}$**	**$NbC_{0.5}N_{0.5}$**
C_{11} (GPa)	546	732	516	661
C_{12} (GPa)	112	153	75	126
C_{44} (GPa)	175	129	111	134
B (GPa)	256 255[10]	328 360[12]	222	304 306[12]
G (GPa)	191	183	147	177
E (GPa)	459	463	361	446
v	0.202	0.264	0.229	0.256
Hv (GPa)	27.2	18.2	19.6	18.8
B/G	1.34	1.79	1.51	1.71
Cauchy pressure (GPa)	−63.2	23.5	−36.2	−8.2

Several empirical indices can be used to evaluate the brittleness or ductility of materials. The Poisson's ratio v is defined as the bonding indicator of materials. If $v > 0.26$, the materials are ductile [49], whereas when the v is ~ 0.1, implying the materials are covalent crystals. Among the four $MC_{0.5}N_{0.5}$ solids, the v values of 0.20 M = Hf and 0.23 M = Cr imply that these two materials are brittle, whereas the v values of the other two solids for M = Ta (0.26) and M = Nb (0.26) indicate these are ductile. The Pugh index (B/G) is generally used to predict the brittleness or toughness of materials. If $B/G > 1.75$, the solid is tough, otherwise it is brittle ($B/G < 1.75$) [27]. The Pugh ratios of $MC_{0.5}N_{0.5}$ are 1.34 (M = Hf), 1.79 (M = Ta), 1.51 (M = Cr) and 1.71 (M = Nb), respectively, indicating that the $MC_{0.5}N_{0.5}$ are brittle except $TaC_{0.5}N_{0.5}$, Hf-containing carbonitride presents maximum brittleness. Interestingly, the $NbC_{0.5}N_{0.5}$ solid is closely related to the threshold value, making it more likely to exhibit brittle to ductile transformation. The evolution of chemical bonding can be predicted by Cauchy pressure (C_{12}-C_{44}). A positive Cauchy pressure indicates the materials exhibit ductility and are dominated by metallic bonding. The more positive the Cauchy pressure, the stronger metallic bond and the greater the toughness. Conversely, negative values of Cauchy pressure indicate that the materials mainly composed of covalent bonds. The three $MC_{0.5}N_{0.5}$ solids all exhibit negative Cauchy pressure except $TaC_{0.5}N_{0.5}$, and a stronger covalent bond and greater brittleness are indicated by the more negative Cauchy pressure for the $HfC_{0.5}N_{0.5}$ solid (Table 3).

The Ti/MCN interfacial models are built in accordance with the above convergence testing and XRD analysis results, and Ti (1 0 1)/MCN (2 2 0) is the orientation relationship. Fig. 1d displays the side view of the model. For convenience, the interface models are named as follows: the Ti/HfCN interface is named Hf (Ti), the Ti/TaCN interface is named Ta (Ti), and the Ti/NbCN interface is named Nb (Ti). Here, the Cr (Ti) interfacial model was ignored due to the unsatisfactory cohesive strength results from the scratch tests in Fig. 5. After the interface is built, the work of adhesion (W_{ad}), which is the reversible

work necessary to split an interface into two free surfaces, can be used to qualitatively characterize the binding strength between the interfaces. Stronger bonding between interface atoms is accompanied by the larger W_{ad}. The W_{ad} can be obtained from the equation [24]:(8)Wad=1A(ETi+EMCN-ETi/MCN)Here, $E_{Ti/MCN}$ represents the total energy of the interface system, and the total energy of the Ti and MCN are represented by E_{Ti} and E_{MCN}, respectively, after full relaxation, A is the area of the interface.



1. Download: Download high-res image (2MB)
2. Download: Download full-size image

Fig. 5. SEM images, acoustic emission (AE) signal and corresponding EDS analysis of the scratch tracks for HfCN coating (a-a_1, a_2 and a_3), TaCN coating (b-b_1, b_2 and b_3), CrCN coating (c-c_1, c_2 and c_3) and NbCN coating (d-d_1, d_2 and d_3).

Table 4 displays the values of W_{ad} and interface distance (d_0). It can be concluded that the Hf (Ti) and Ta (Ti) interface presents the highest W_{ad} values, suggesting that they have the strongest adhesive strength among all interfaces.

Table 4. The interfacial ideal d_0 and W_{ad} for Ti (1 0 1)/MCN (2 2 0) interfacial structure models.

Interfaces	d_0 (Å)	W_{ad} (J/m^2)
Hf (Ti)	2.350	5.7
Ta (Ti)	2.279	5.7
Nb (Ti)	2.139	3.7

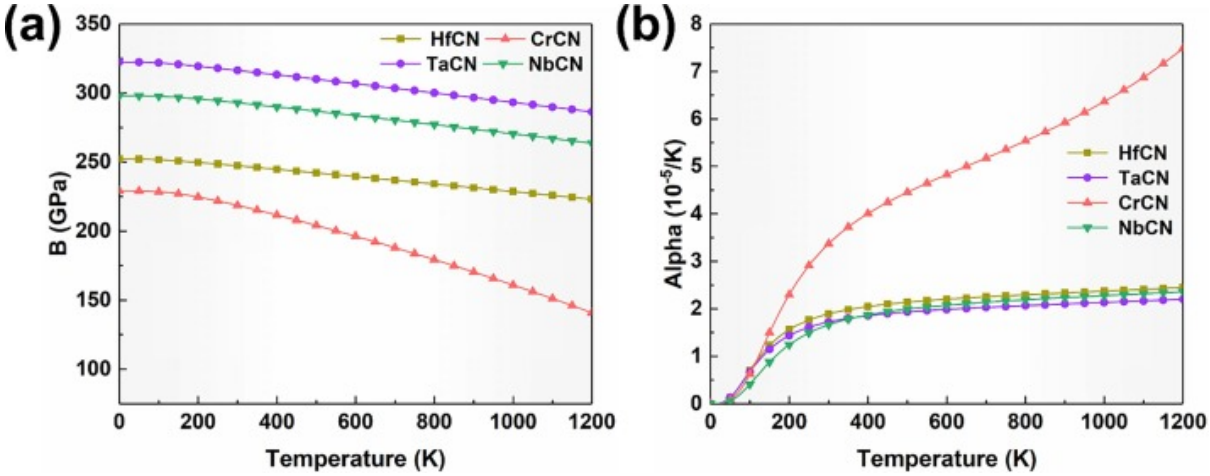
Fig. 5 shows the scratch behavior of the MCN coatings. The SEM images of MCN coatings are shown in Fig. 5a-d, and the corresponding high magnification SEM images and EDS surface scan of the selected regions are shown in Fig. 5a1-d1 and Fig. 5a3-d3, respectively. Fig. 5a2-d2 display the acoustic emission (AE) signal in relation to the applied normal load (F_n). The cohesive strength of the coating is commonly represented by L_{c1}, which is typically defined as the lower load that the coating begins to crack or partial spallation [28]. The interfacial adhesive strength of the coating is commonly represented by L_{c2}, indicating the upper critical load that the beginning of continuous substrate exposure, or areas of total coating failure [50]. For MCN coatings, the initial cracking of the coatings occurred at ~1.04 mm (HfCN, Fig. 5a), ~0.92 mm (TaCN, Fig. 5b), ~0.62 mm (CrCN, Fig. 5c) and ~0.78 mm (NbCN, Fig. 5d), respectively, which are defined as L_{c1} values. Then, a sudden drop in the AE curves appeared with the progressive loading, and the coatings almost removed from the matrix at the areas, which are identified as L_{c2} and corresponding to the exposure of Ti element in the substrate according to the SEM and EDS analysis. Notably, the tensile cracking typically precedes cohesive failure (such as chipping) of coatings, which is consistent with this study, meaning that, in all coatings, chipping around the edge of the scratch tracks was observed subsequent to the appearance of L_{c1}. In Table 5, it is evident that the HfCN coating exhibits the largest L_{c1} value (~16.7 N), L_{c2} value (~55.3 N) and CPR value (~921) value, which indicates the excellent crack propagation resistance, corresponding to its larger W_{ad} value as shown in Table 4.

Table 5. Scratch tests of the MCN (M=Hf, Ta, Cr, Nb) coatings.

Coatings	L_{c1} (N)	Location, L_{c1} (mm)	L_{c2} (N)	Location, L_{c2} (mm)	CPRs
HfCN	~16.7	~1.04	~55.3	~3.46	~921
TaCN	~14.8	~0.92	~30.3	~1.89	~229
CrCN	~9.9	~0.62	~28.0	~1.75	~179
NbCN	~12.4	~0.78	~24.5	~1.53	~149

A material's strength can typically be estimated using the bulk modulus B, since higher strength corresponds with larger bulk modulus [41]. As shown in Fig. 6a, the $CrC_{0.5}N_{0.5}$ exhibits noticeable softening behavior with increasing temperature after T > 200 K, presenting a sharp decline in the bulk

modulus curve. The other three $MC_{0.5}N_{0.5}$ solids exhibit similar trends. The B values of $TaC_{0.5}N_{0.5}$ are consistently higher than the other systems over the total temperature region, indicating the $TaC_{0.5}N_{0.5}$ has the strongest strength, giving it a high temperature application advantage.

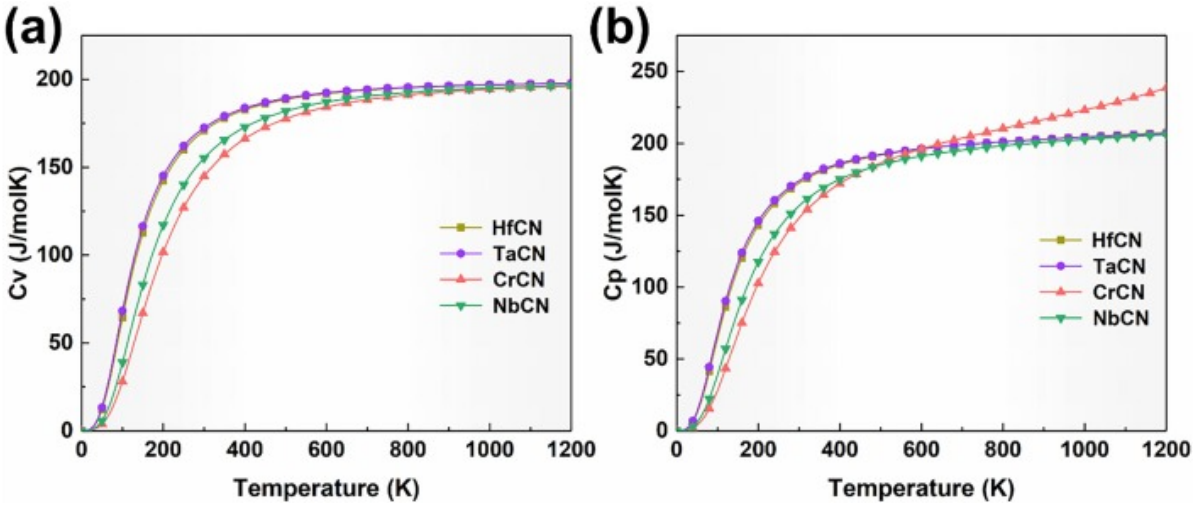


1. Download: Download high-res image (231KB)
2. Download: Download full-size image

Fig. 6. The bulk modulus (a) and thermal expansion coefficient (10^{-5}/K) (b) for MCN (M=Hf, Ta, Cr, Nb).

Fig. 6b shows the variation of the thermal expansion coefficient with temperature. At T < 300 K, the thermal expansion coefficients of the four $MC_{0.5}N_{0.5}$ solids increase dramatically, and then grows slowly, except for the $CrC_{0.5}N_{0.5}$ solid continues to show a rapid increase. For $MC_{0.5}N_{0.5}$ (M = Hf, Ta, Nb) solid, it is more challenging to expand with a lower thermal expansion coefficient. The $MC_{0.5}N_{0.5}$ with lower thermal expansion is beneficial for high-temperature applications owing to the relatively low thermal expansion coefficient of the Ti alloy substrate [51].

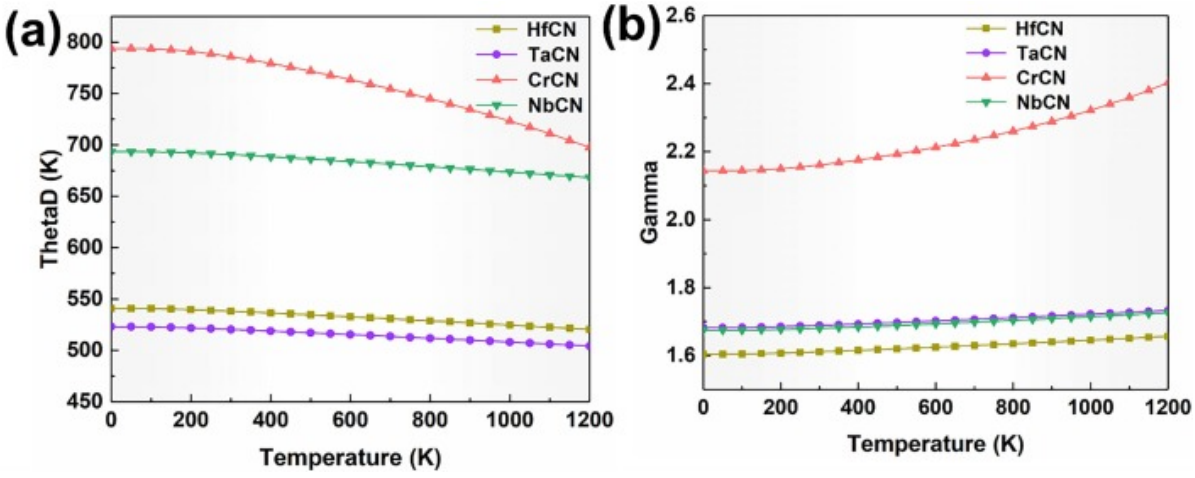
Heat capacity is one of the most important thermodynamic characteristics, which is crucial for connecting thermodynamics and dynamics [27]. Fig. 7a shows that the C_v values of the $MC_{0.5}N_{0.5}$ solids are highly sensitive to temperature at T < 500 K, increasing rapidly. Then, the C_v values close to a constant at T > 500 K, meeting the well-known Dulong-Petit limit. The C_v values of $HfC_{0.5}N_{0.5}$ and $TaC_{0.5}N_{0.5}$ are always very close and higher than the other two solids over the whole temperature range. Essential information on the vibrational properties of materials can be obtained from their heat capacity at constant pressure (C_p). Fig. 7b displays the C_p values of $MC_{0.5}N_{0.5}$ rapidly increase at T < 450 K, and then increase slowly at high temperatures. Overall, the C_p value of $HfC_{0.5}N_{0.5}$ is almost the same as this for $TaC_{0.5}N_{0.5}$. At high temperatures, the C_p does not at a constant, the low coefficient of thermal expansion α (Fig. 6b) accounts for the small difference, which can be understood easily by the equation: $C_p - C_v = (3\alpha)^3BTV$ [27], [49].



1. Download: Download high-res image (234KB)
2. Download: Download full-size image

Fig. 7. The heat capacity at constant volume C_v (J/molK) (a) and constant pressure C_p (J/molK) (b) as a function of temperature for MCN (M=Hf, Ta, Cr, Nb).

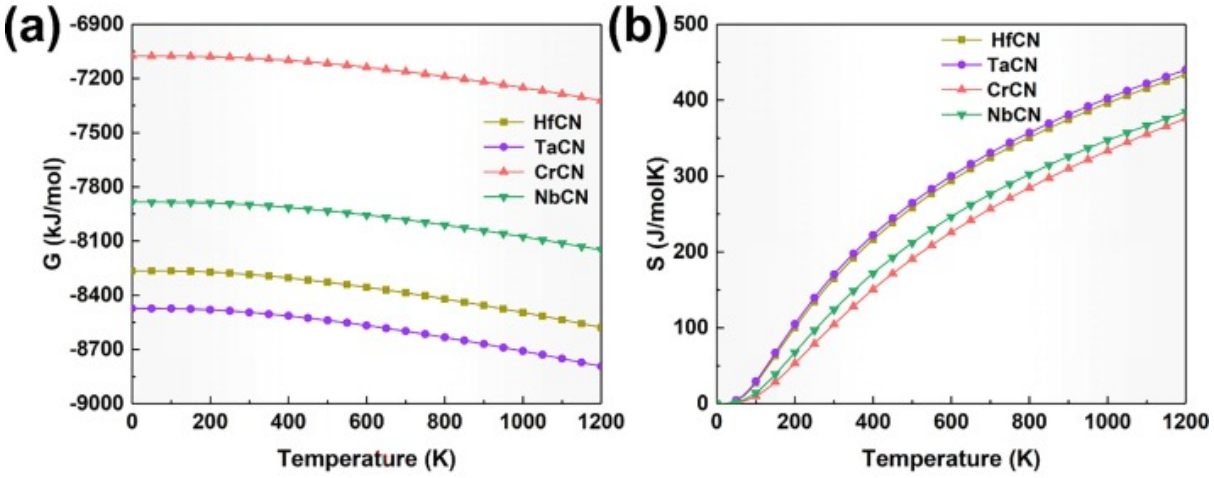
The Debye temperature is closely related to the thermodynamic stability of a material. The variation curves of the Debye temperature of $MC_{0.5}N_{0.5}$ solids at different temperatures are shown in Fig. 8a. For $MC_{0.5}N_{0.5}$ (M=Hf, Ta, Nb) solids, the Debye temperature follows a similar variation trend, slowly decreasing as temperature increases. At low temperatures, the Debye temperature for $CrC_{0.5}N_{0.5}$ solid decreases slowly, and then drop slightly quick with increasing temperature. The Debye temperature values for $CrC_{0.5}N_{0.5}$ are greater than those for the other three solids over the entire temperature range, which means the $CrC_{0.5}N_{0.5}$ has higher thermal conductivity. Overall, there is little correlation between temperature T and Debye temperatures. The Grüneisen parameter γ as a function of different temperatures for $MC_{0.5}N_{0.5}$ are displayed in Fig. 8b. The γ values of the four $MC_{0.5}N_{0.5}$ solids increase with the increasing temperature. In the whole temperature range, the γ value of $CrC_{0.5}N_{0.5}$ is highest, since the larger pressure derivative B'_0 of the bulk modulus of $CrC_{0.5}N_{0.5}$. According to the results, there is no discernible relationship between temperature T and the Grüneisen parameter γ.



1. Download: Download high-res image (234KB)
2. Download: Download full-size image

Fig. 8. The temperature dependence of the Debye temperature (a) and Grüneisen parameter Gamma (b) of MCN (M=Hf, Ta, Cr, Nb).

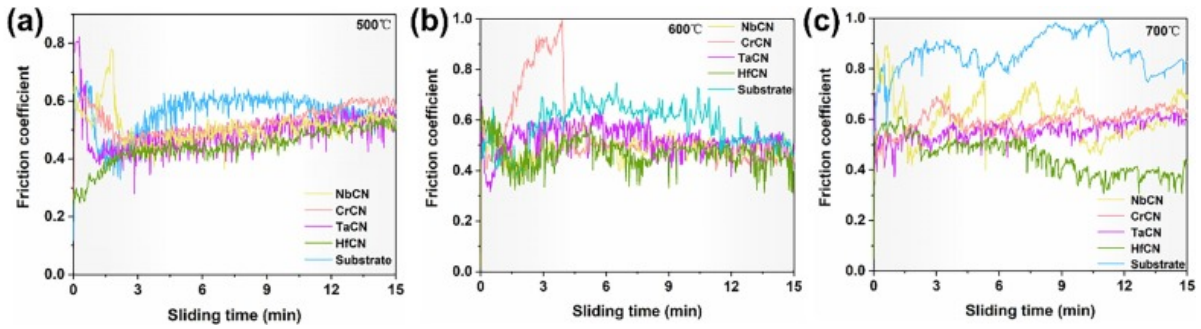
More negative Gibbs free energy (G) and a higher entropy (S) indicate a system that is more thermodynamically stable. As shown in Fig. 9, the $HfC_{0.5}N_{0.5}$ and $TaC_{0.5}N_{0.5}$ solids are more stable than the other two solids, which is related to their lower G value (Fig. 9a) and higher S values (Fig. 9b).



1. Download: Download high-res image (253KB)
2. Download: Download full-size image

Fig. 9. The calculated Gibbs free energy (kJ/mol) (a) and entropy S (J/molK) (b) as a function of temperature for MCN (M=Hf, Ta, Cr, Nb).

Fig. 10 shows the coefficient of friction (COF) curves of the coatings at 500 °C, 600 °C and 700 °C, respectively. The COF of the coatings were lower than that of the substrate. The uncoated substrate suffered from severe abrasive wear, which increased the COF with increasing temperature. The coating samples appeared less abrasive wear, and the COF values were reduced correspondingly, as confirmed by the COF values of the coatings in Table 6. The HfCN and TaCN coating samples show low and stable COF curves except in some initial run-in stage (~0–3 min, Fig. 10a-c) owing to their good adhesion strength and low thermal expansion coefficient with the substrate, as well as the low S entropy values. The COF curves of the two coatings exhibited the similar trend with increasing temperatures, indicating they had good anti-wear properties at high temperatures. However, as the M=Cr and Nb coatings, the COF values increased to ~0.62 and 0.65 at 700 °C (Fig. 10c). It can be attributed to the reduction in the adhesion strength and the large thermal expansion coefficient with the substrate, resulting in the coatings peeled away from the substrate during the sliding friction. Additionally, the three-body wear may result from the abrasive debris that is produced when the coatings degrade and flake away from the substrate. As a result, the oscillation amplitude and COF values of the friction coefficient curves grow substantially, exhibiting in higher COF values and more unstable than those at 500 °C (Fig. 10a) and 600 °C (Fig. 10b).



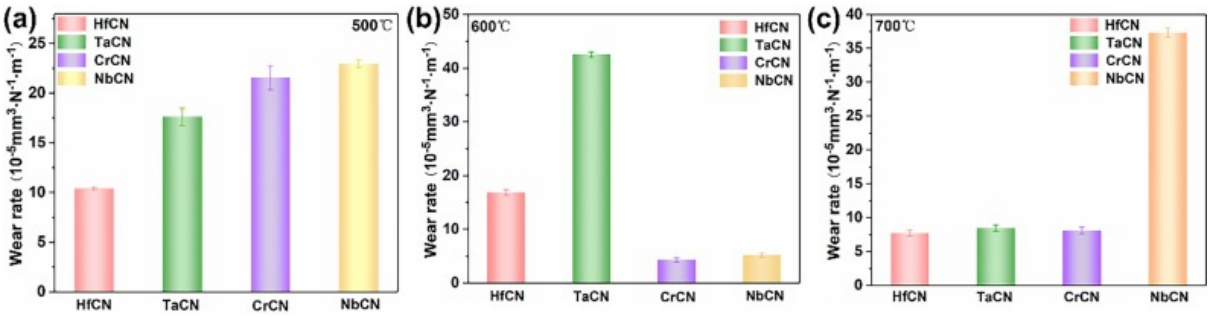
1. Download: Download high-res image (324KB)
2. Download: Download full-size image

Fig. 10. Coefficient of friction of all coatings and the substrate at (a) 500 °C, (b) 600 °C and (c) 700 °C after the wear tests.

Table 6. The average friction coefficient, wear depth and wear width of each coating at 500 °C, 600 °C and 700 °C.

Coatings	500 °C			600 °C			700 °C		
	COF	Wear depth (μm)	Wear width (mm)	COF	Wear depth (μm)	Wear width (mm)	COF	Wear depth (μm)	Wear width (mm)
HfCN	0.45	9.66 ± 0.30	0.45 ± 0.02	0.46	12.2 ± 0.56	0.57 ± 0.01	0.46	4.25 ± 0.20	0.76 ± 0.02
TaCN	0.49	13.9 ± 0.25	0.53 ± 0.03	0.54	28.4 ± 0.35	0.62 ± 0.01	0.57	7.31 ± 0.65	0.48 ± 0.02
CrCN	0.54	14.4 ± 0.24	0.62 ± 0.02	0.47	6.24 ± 0.12	0.29 ± 0.02	0.62	6.66 ± 0.24	0.51 ± 0.04
NbCN	0.51	16.2 ± 0.20	0.59 ± 0.01	0.50	5.99 ± 0.16	0.36 ± 0.02	0.65	27.1 ± 0.40	0.57 ± 0.01

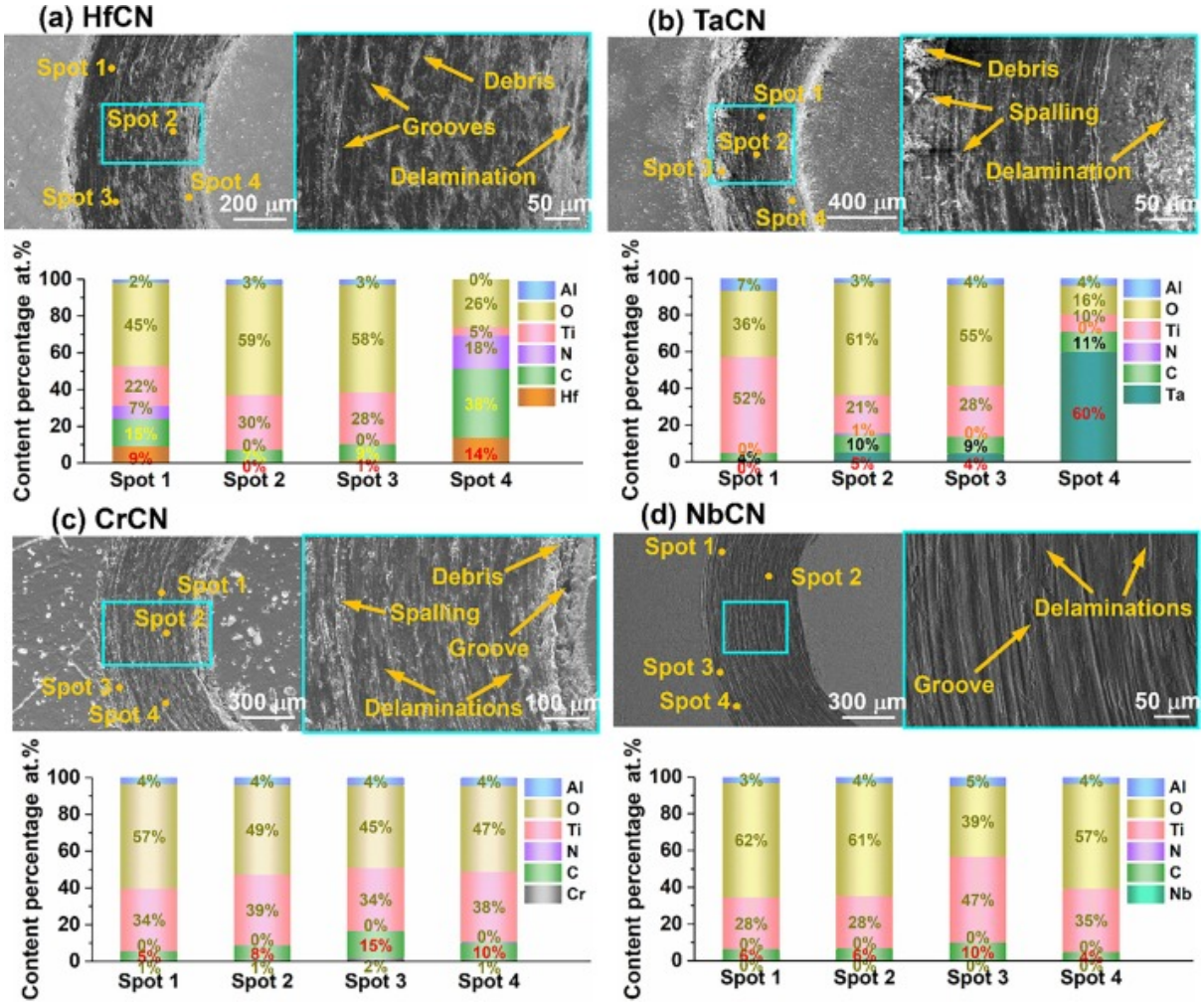
The wear rates of MCN samples at 500 °C, 600 °C and 700 °C are shown in Fig. 11. At different high temperatures, the coatings always exhibited the wear rate of an order of ~10^{-4} $mm^3N^{-1}m^{-1}$. The wear rate of HfCN and TaCN coatings increased from 500 °C to 600 °C, and then reduced from 600 °C to 700 °C. However, the CrCN and NbCN coatings exhibit the opposite trend with the increasing temperature. HfCN and TaCN coatings have better wear resistance than CrCN coating, which corresponds to their higher adhesion strength W_{ad} and B, low α and COF values as shown in Fig. 6. The wear rate of HfCN coatings is about two times lower than that of CrCN at 500 °C, and about five times lower than that of CrCN at 700 °C. Although the CrCN presents a lower wear rate than HfCN at 600 °C, it can be attributed to the lower hardness of CrCN occurs certainly soften during the sliding friction as shown in the theoretical calculation in Table 3, resulting in the change of wear mechanism (explained later) of CrCN coatings at 600 °C, which lead to less material being removed out of the surface of the wear track.



1. Download: Download high-res image (194KB)
2. Download: Download full-size image

Fig. 11. The wear rate of MCN coatings at 500 °C (a), 600 °C (b) and 700 °C (c), respectively.

The low magnification and high magnification SEM morphology of wear marks on MCN (M = Hf, Ta, Cr, Nb) samples at 500 °C are shown in Fig. 12. Clearly, the worn surface of all samples revealed the existence of wear debris and parallel furrows. The reasons for this are as follows: firstly, the two-body wear caused by the asperities formed on the surface of both coatings and Si_3N_4 balls, which caused the ball to plow into the surfaces of samples. Secondly, amounts of debris would move between the ball and the surface of samples during the friction and wear process, and these debris experienced a progressive increase in hardness and an irregular shape due to deformation and work hardening, which leads to increased contact stress between the debris and the friction interfaces. Eventually, abrasive debris causes the samples to be plowed under. Thus, the presence of wear debris and parallel furrows indicate that the wear mechanism of all samples involves abrasive wear.



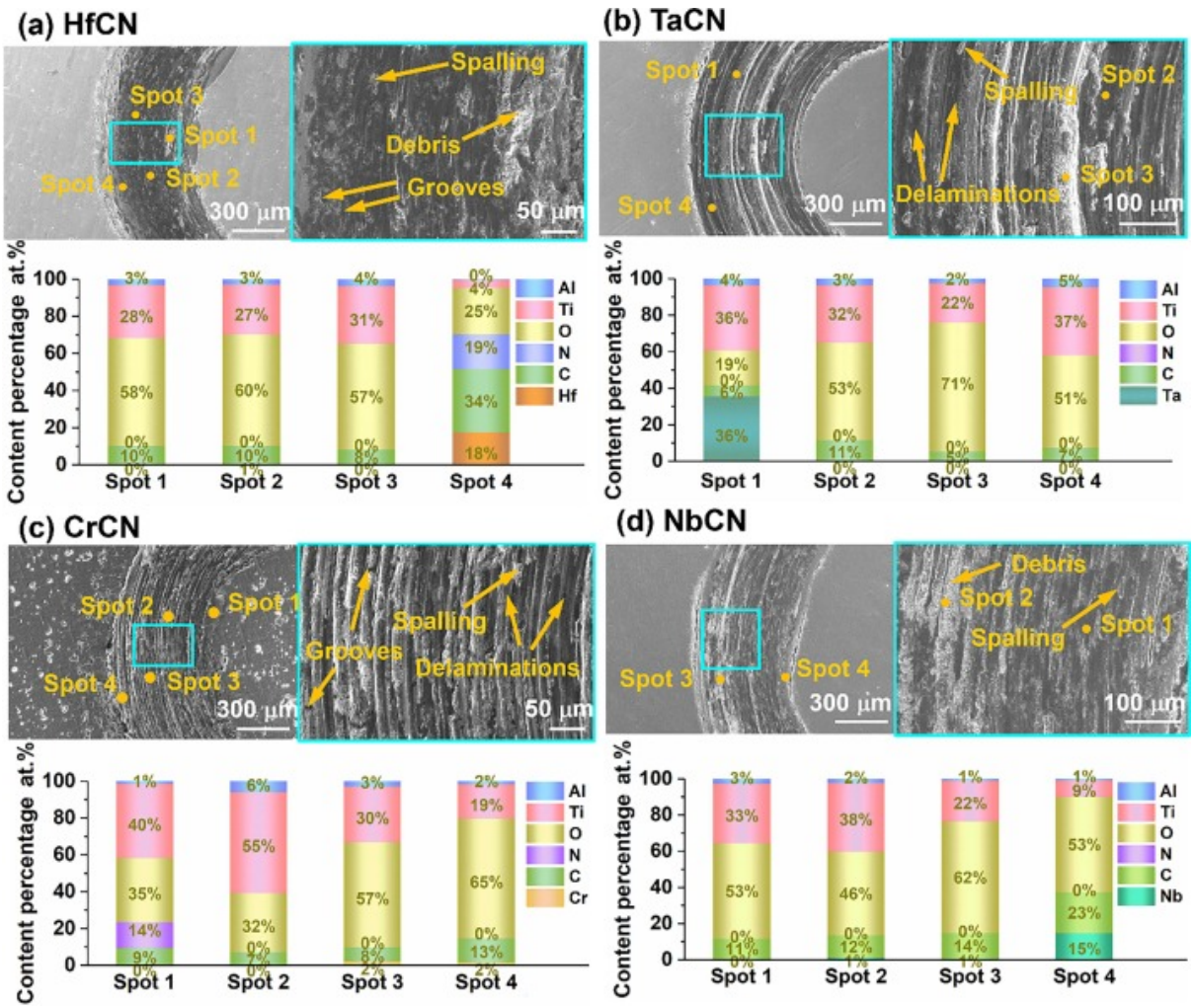
1. Download: Download high-res image (1MB)
2. Download: Download full-size image

Fig. 12. The SEM images and corresponding EDS analysis of HfCN coating (a), TaCN coating (b), CrCN coating (c), NbCN coating (d) at 500 °C.

Meanwhile, the EDS points analysis detected high O content on the worn surface of all samples, and the debris was primarily composed of Ti, O, and C, indicating that they were probably oxide particles.

This indicates that all samples present an oxidative wear mechanism caused by the frictional heat effect during repeated sliding. Among these four wear surfaces, the worn surfaces of HfCN (Fig. 12a) and TaCN (Fig. 12b) samples were detected with Hf, C, N, and Ta, C, N, respectively, which confirmed the coatings were not worn out completely. Besides, the worn surface of CrCN (Fig. 12c) and NbCN (Fig. 12d) samples show wide and deep furrows, suggesting an increased role of abrasive wear of CrCN and NbCN samples compared to HfCN and TaCN samples. The worn surface of the latter two shows peeling, with less plowing, and the worn surfaces will stick to one another and form bonding points under the reciprocating sliding action, the bonding points may be severed during the wear process, causing material loss and pit formation. Based on these, it can be concluded that the main wear mechanism of HfCN and TaCN samples was adhesive wear and oxidation wear, and that of CrCN and NbCN samples was abrasive wear and oxidation wear at 500 °C.

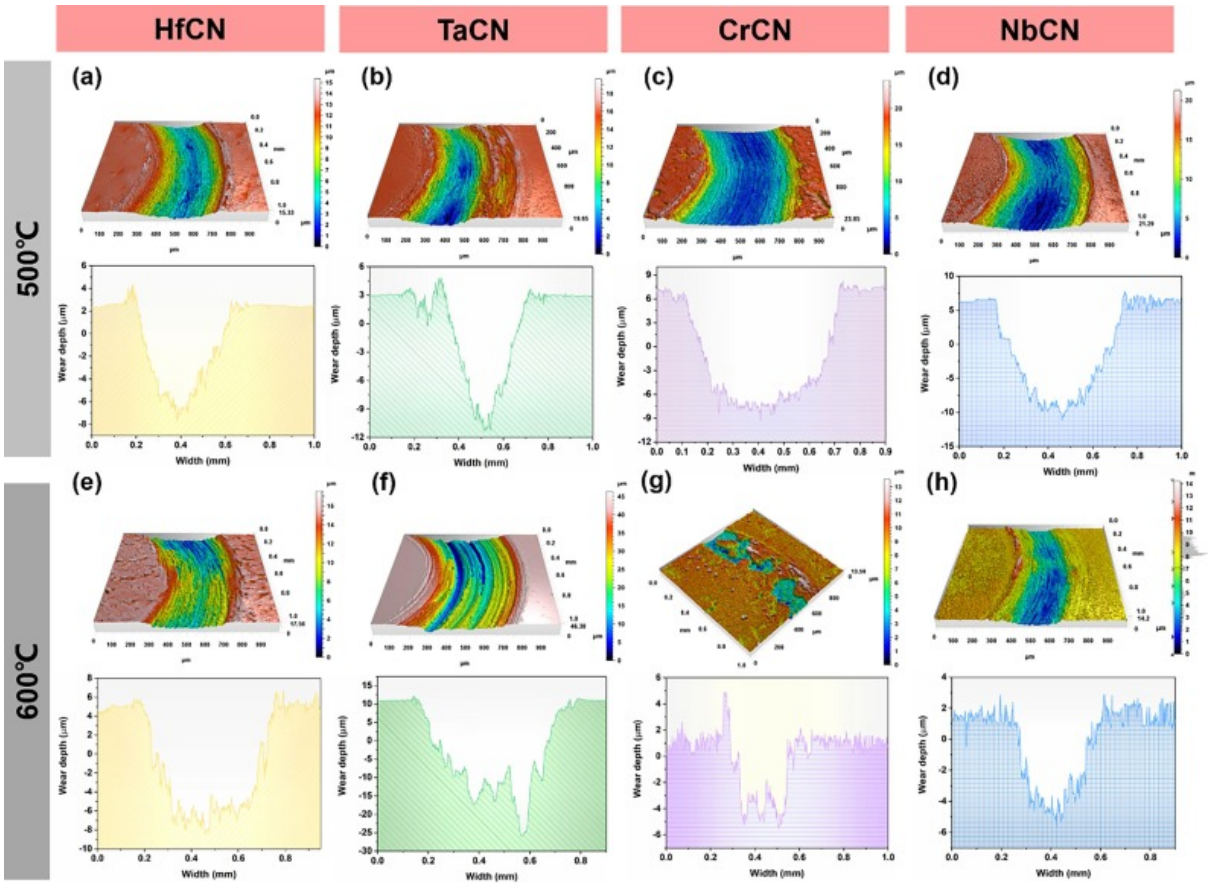
Fig. 13 shows SEM images and EDS point scans of MCN coatings. In the case of HfCN (Fig. 13a) and TaCN (Fig. 13b) coatings, tribo-products are observed to eject from the wear tracks and accumulate around them during the wear process, indicative of a typical third-body abrasive wear mechanism. Subsequently, these wear debris locally abrade the coating surface, accelerating ploughing action. This process results in the formation of numerous grooves and spalling on the wear tracks, ultimately increasing the wear rate. Meanwhile, there are many minor flats in their wear tracks, are typically characteristic of adhesion wear. The EDS analysis indicated that the tribo-products mainly consisted of Hf, Ti, O for HfCN and Ta, Ti, O for TaCN, suggesting that the coatings had not completely failed, with only part of the matrix being exposed. The wear mechanisms observed for these coatings were predominantly abrasive wear and oxidation wear. In contrast, for CrCN (Fig. 13c) and NbCN (Fig. 13d) coatings, the tribo-products on the wear tracks exhibited tendencies towards adhesion and plastic deformation. This behavior is attributed to increased ductility and reduced hardness of the coatings at elevated temperatures. Although the surface of wear tracks appears relatively smooth compared to that of HfCN and TaCN coatings, EDS analysis revealed abundant O and Ti elements on the wear tracks, with scarce presence of Cr or Nb elements, indicating complete coating failure. The predominant wear mechanisms observed were adhesion wear and oxidation wear. These results suggest that the higher wear rate of HfCN and TaCN coatings at 600 °C is primarily attributed to a shift in wear mechanism. Nonetheless, HfCN and TaCN coatings still demonstrated superior wear resistance compared to the other two samples. At high tempertures, the MCN ceramic coatings undergo thermal expansion as shown in Fig. 6, which can lead to thermal mismatch stresses due to the coefficients of thermal expansion (CTE) of the ceramic coatings and substrate differ significantly, and the thermal cycling during the sliding wear test can further increase the thermal stress, and accelerates the spalling of the coating, as well as accumulating fatigue damage [52], as confirmed in the EDS analysis results of CrCN and NbCN coatings.



1. Download: Download high-res image (1MB)
2. Download: Download full-size image

Fig. 13. The SEM images and corresponding EDS analysis of HfCN coating (a), TaCN coating (b), CrCN coating (c), NbCN coating (d) at 600 °C.

Fig. 14 shows the wear tracks 3D profiles and corresponding 2D profiles of MCN coatings at 500 °C and 600 °C, respectively. The HfCN (Fig. 14a) and TaCN (Fig. 14b) samples exhibited a smaller width (~447.6 μm, ~527.0 μm) and depth (~9.7 μm, ~13.9 μm) compared with that of CrCN (Fig. 14c) and NbCN (Fig. 14d) coatings, combined with their low COF values, S entropy values, thermal expansion coefficient with Ti substrate and excellent adhesion strength, confirming the superior wear resistance of the HfCN and TaCN coatings. However, at 600 °C, the 3D profile of the wear tracks of HfCN (Fig. 14e) and TaCN (Fig. 14f) samples shows the accumulation of material around the wear tracks, and the wear tracks of CrCN (Fig. 14g) and NbCN (Fig. 14h) samples looked smoother and without tribo-products accumulated around the tracks, which corresponds to the wear rate values of them. The higher wear rate of HfCN and TaCN samples at 600 °C was mainly attributed to the transformation of wear mechanisms from adhesion wear at 500 °C to abrasive wear at 600 °C, nevertheless, the HfCN and TaCN coatings had not occur worse wear than CrCN and NbCN samples as the EDS analysis in Fig. 13.

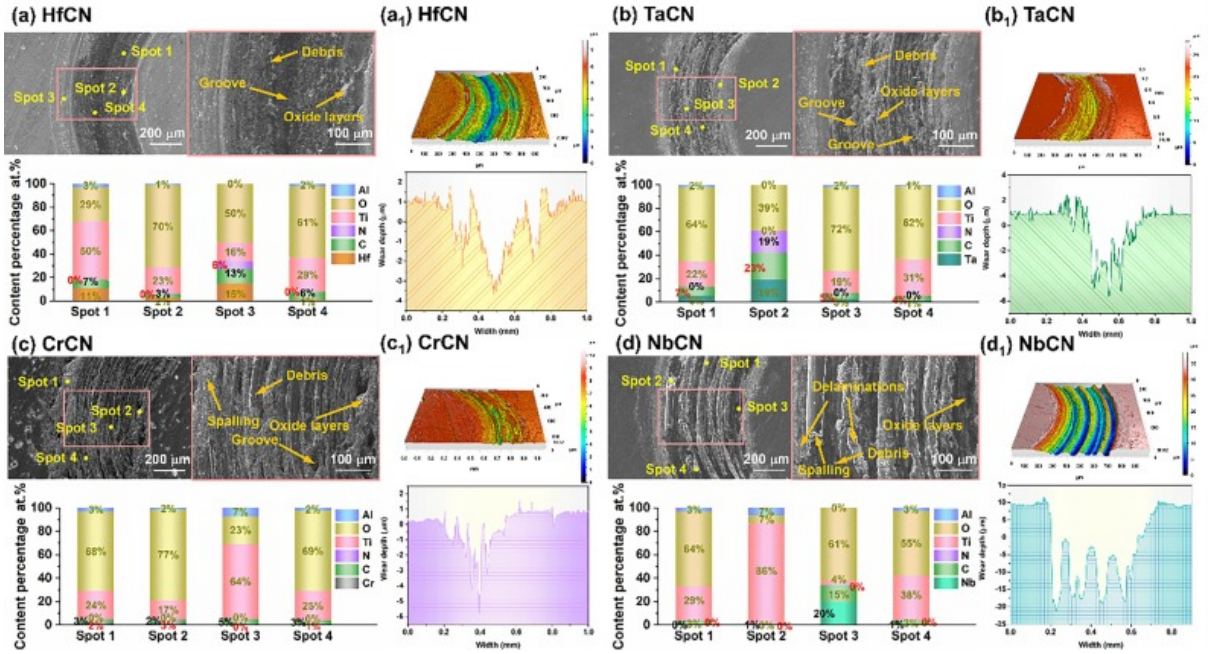


1. Download: Download high-res image (829KB)
2. Download: Download full-size image

Fig. 14. The 3D and 2D profiles of wear tracks of the HfCN coatings (a, e), TaCN coatings (b, f), CrCN coatings (c, g) and NbCN coatings (d, h) at 500 °C (a-d), 600 °C (e-h), respectively.

Fig. 15 shows the worn morphologies of MCN coatings at low and high magnifications at 700 °C. Much wear debris accumulated around the external side of the wear tracks (Fig. 15b-d) except the case of the HfCN coatings (Fig. 15a). For HfCN coating, slight delamination was observed at the external side of the wear track, and there was an increase in the adhesion and amount of wear debris within the wear track, while the size of the debris decreased compared to that of in the other coatings shown in Fig. 15b-d. A large continuous tribo-oxide layer was formed on the wear track of HfCN coating, and the coating was not totally worn out, as confirmed by the high O content and low Hf content in the EDS analysis. The main wear mechanisms were adhesion wear and oxidation wear. For the other coatings, the outer edge of the wear tracks exhibited severe delamination, an increase in the size and amounts of debris. The EDS analysis at the external edge of the wear track further confirmed the coatings had delaminated with lower M content on the wear tracks, high O and Ti, Al content from the matrix. Besides, many grooves were formed within the wear tracks of CrCN (Fig. 15c) and NbCN coatings (Fig. 15d), suggesting abrasive wear and oxide wear were their main wear mechanism. Meanwhile, the spalling was observed on the tribological surface as the result of plastic shear strain accumulated during the delamination process. The main wear mechanism of the three coatings was abrasive wear, adhesion wear and oxidation wear. The wide and depth of wear tracks of HfCN (Fig. 15a1), TaCN (Fig. 15b1) and CrCN (Fig. 15c1) coatings were lower than that of at 500 °C and 600 °C, respectively, which correspond to their relatively smooth wear tracks. According to the above analysis, it can be

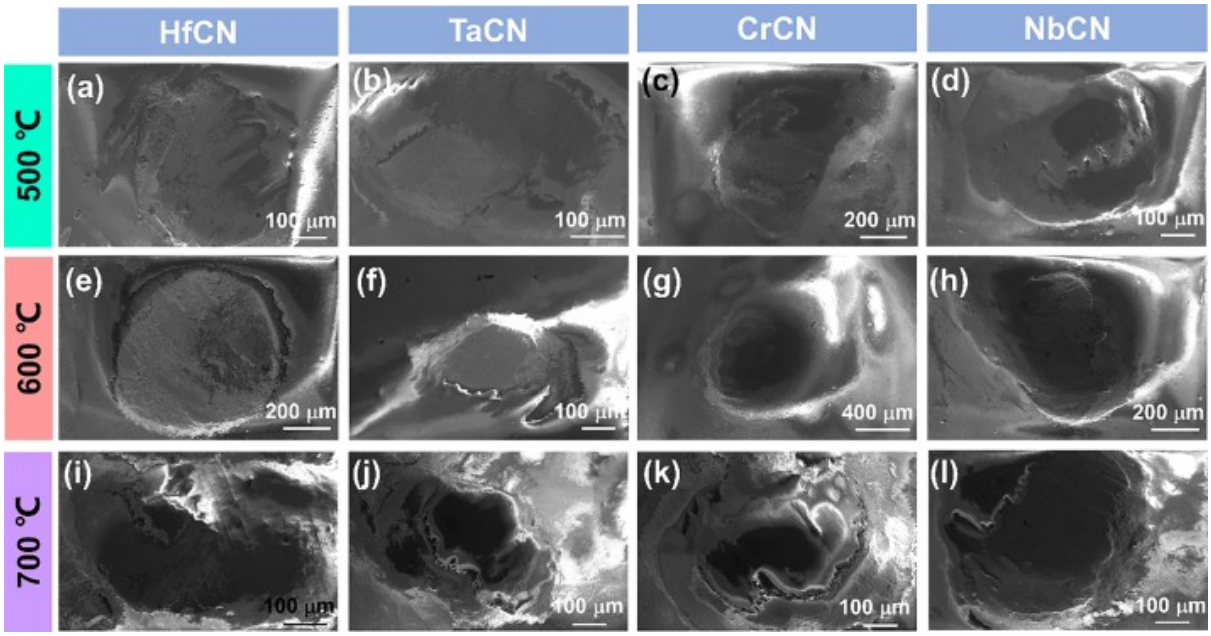
concluded that good adhesion strength between the coating and the matrix, and superior thermodynamic stability (lower G value and higher S value in Fig. 9) are mainly related to the wear behavior of the coatings, in turn, the microstructure and composition of the coatings effected the wear behavior of the coatings.



1. Download: Download high-res image (928KB)
2. Download: Download full-size image

Fig. 15. SEM images and EDS analysis, wear tracks 3D and 2D profiles of HfCN coating (a, a1), TaCN coating (b, b1), CrCN coating (c, c1) and NbCN coating (d, d1), respectively, at 700 °C.

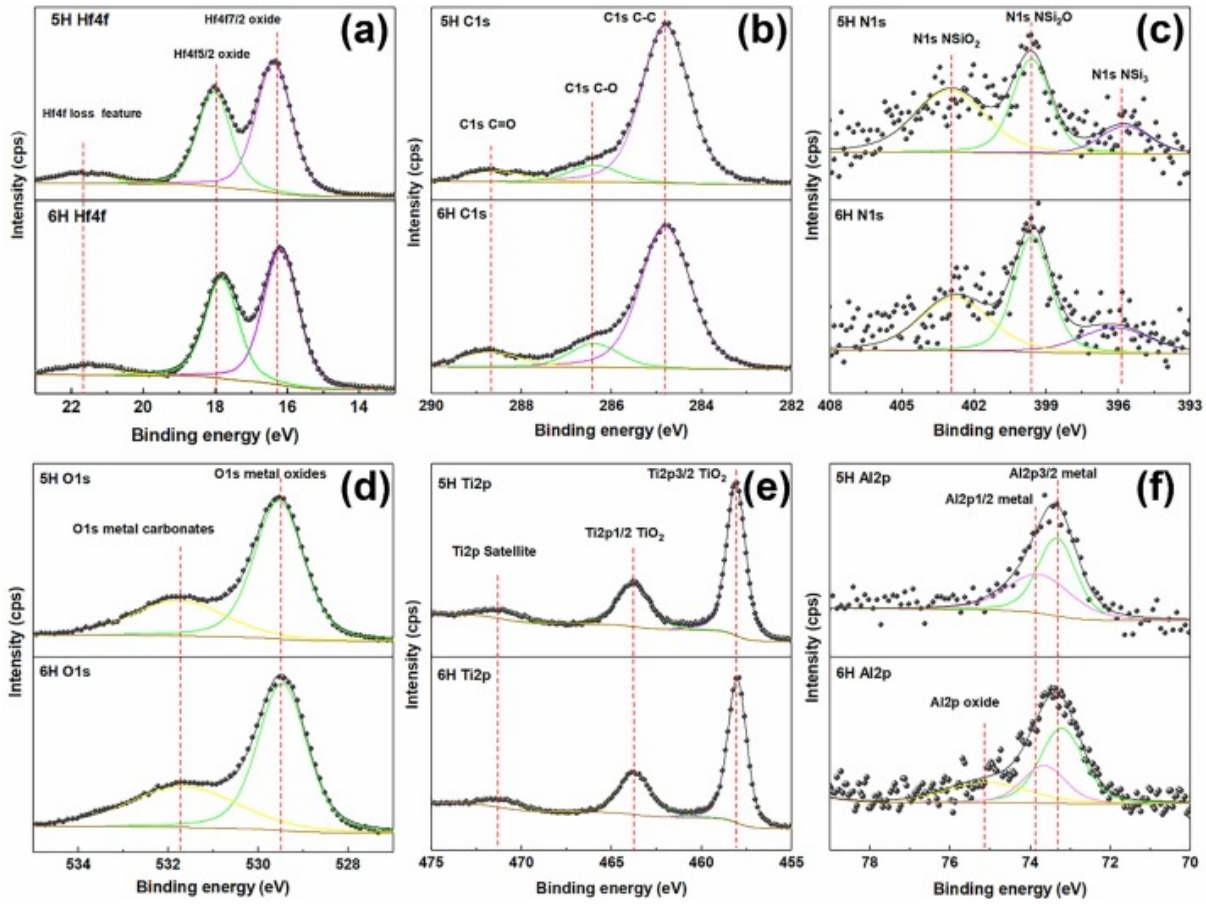
Fig. 16 shows the wear scars on the Si_3N_4 counterpart balls at 500 °C, 600 °C and 700 °C, respectively. Obviously, the size of wear scar of Si_3N_4 ball significantly decreased with increasing tribological temperatures (from 500 °C to 700 °C). The wear scar exhibited a clear edge as a circular shape at 500 °C (Fig. 16a-d), and then revealed a more oval-shaped image and darker color at higher temperatures (600 °C (Fig. 16e-h), 700 °C (Fig. 16i-l)). The wear debris accumulated around the outer edge of wear scar, which was consisted of the materials from the surface the wear samples and the counterpart ball Si_3N_4 as the XPS analysis result in Fig. 16c. Combined with the above SEM images of MCN coatings at different temperatures (Fig. 12, Fig. 13&15), it can be concluded that the darker color of Si_3N_4 wear scar was accompanied with the more severe adhesion wear of the coatings. For the same coating, the color of the counterpart ball wear scar was gradually darker with increasing temperature, suggesting that the adhesive wear aggravated as the temperature increased.



1. Download: Download high-res image (591KB)
2. Download: Download full-size image

Fig. 16. Wear scar on the Si_3N_4 counterpart balls as the result of testing against the MCN coatings at 500 °C (a-d), 600 °C (e-h) and 700 °C (i-l), respectively.

To further investigate the wear resistance of HfCN coatings at high temperatures, the chemical bonding state of the wear tracks on the surface of the HfCN samples were studied by the XPS analysis as shown in Fig. 17. The Hf element shows two common oxidation states under different temperatures, Hf5/2 oxide and Hf7/2 oxide (Fig. 17a) [13], and the binding energy of them are located at 17.83 eV and 16.18 eV, respectively. The peak of loss feature Hf4f was located at 21.58 eV. And the intensity of the Hf4f oxide peaks is similar at different temperatures, indicating the similar degree of oxidation with increasing temperatures. Similarly, the peaks of C1s, N1s, O1s and Ti2p show the same trend of oxidation strength variation with increasing temperatures. However, for C element (Fig. 17b), the peak intensity of C1s C–C (284.78 eV) was higher than that of C1s C-O (286.38) and C1s C O (288.73 eV) [53], which played a lubricating role in the wear process and was accordance with the low wear rate in Fig. 11. The three peaks of N1s were located at 402.83 eV, 399.58 eV and 396.18 eV, respectively (Fig. 17c), and were identified as $NSiO_2$, NSi_2O [41] and NSi_3. The results confirmed transfer occurred from the Si_3N_4 counter pair to the coating during the tribology. In Fig. 17d, the peak of O1s metal oxides at 531.68 eV showed stronger intensity than that of O1s metal carbonates at 529.48 eV [53], indicating the severe oxidation during the wear process at different temperatures. And the Ti2p in Fig. 17e were mainly consisted with the Ti2p satellite (471.38 eV), Ti2p1/2 TiO_2 (463.73 eV) and Ti2p3/2 TiO_2 (458.03 eV) [54], which indicating the part of the substrate was exposed and reacts with oxygen during the high temperatures friction, and was also consistent with the results of the wear mechanism in Fig. 12, Fig. 13. For Al 2p in Fig. 17f, the Al2p1/2 metal (73.68 eV) and Al2p3/2 (73.43 eV) metal were mainly present in the different high temperatures, whereas, Al2p oxide at 75.08 eV [54] could only be detected at 600 °C, explaining that more severe oxidation with increasing temperatures, as well as in accordance with the analysis in Fig. 13.



1. Download: Download high-res image (676KB)
2. Download: Download full-size image

Fig. 17. XPS spectra of the wear tracks on the HfCN samples at 500 °C and 600 °C: (a) Hf4f, (b) C1s, (c) N1s, (d) O1s, (e) Ti2p, (f) Al2p.

4. Conclusions

In summary, in this paper, the elastic constant, adhesion strength, thermodynamic stability and high temperature wear resistance of MCN (M=Hf, Ta, Cr, Nb) using first principles calculations and double glow plasma surface alloying method. The conclusions are as follows:

- (1)

$HfC_{0.5}N_{0.5}$ exhibits the highest hardness (~27 GPa), best ability to withstand reversible deformations under shear stress and more stiffness, while $TaC_{0.5}N_{0.5}$ displays higher ductility.

- (2)

The Ti (1 0 1)/MCN (2 2 0) interface was chosen in accordance with the preferred orientation of the phases, and the interfacial models of Hf (Ti) and Ta (Ti) had higher adhesion strength Wad ~ 5.7 J/m^2, corresponded to their higher critical loads (L_{c1} and L_{c2}) obtained from the scratch tests.

- (3)

For HfCN and TaCN coatings with excellent wear resistance at high temperatures, which is related to their superior thermodynamic stability, e.g. lower thermal expansion coefficient α with the Ti substrate, lower Gibbs free energy G and higher entropy S at high temperature, and their high adhesion strength with Ti substrate.

- (4)

The oxidation wear and adhesive wear mechanism of MCN coatings were gradually severe with

increasing temperature, accompanied by the Al2p oxide occurred at higher temperature (600 °C).

CRediT authorship contribution statement

Mengjuan Yin: Writing – review & editing, Writing – original draft, Methodology, Investigation, Data curation, Conceptualization. **Wenping Liang:** Validation, Resources, Project administration, Funding acquisition. **Qiang Miao:** Supervision, Resources, Methodology, Data curation. **Haiyang Yu:** Writing – review & editing, Visualization, Validation, Data curation. **Yuehao Xu:** Writing – review & editing, Resources, Methodology, Investigation. **Jiumei Gao:** Writing – review & editing, Resources, Methodology, Investigation. **Shijie Sun:** Resources. **Hongmei Jin:** Writing – review & editing, Visualization, Validation, Software, Resources. **Daniel.J Blackwood:** Writing – review & editing, Visualization, Validation, Resources.

Declaration of competing interest

The authors declare that they have no known competing financial interests or personal relationships that could have appeared to influence the work reported in this paper.

Acknowledgements

This work was supported by the National Major Science and Technology Projects of China (Y2022-III-0004-0013), the National Natural Science foundation of China (Grant No 52272065), the Fundamental Research Funds for the Central Universities (NO. NP2022424). M. Yin gratefully acknowledge financial support from China Scholarship Council (CSC). The authors also thank the Structural Metal Alloys Program of the Agency for Science, Technology and Research (ASTAR) (A18B1b0061) for financial support and the National Supercomputing Center (NSCC) Singapore for providing high-performance computing facilities.

Data availability

Data will be made available on request.

References

1. [1]

F. Li, M. Gao, B. Guo

Friction and lubrication mechanism of a new type of anti-magnetic bearing ti60 titanium alloy material[J]

Results Phys., 14 (2019)

Google Scholar

2. [2]

X. Lei, N. Lin, S. Yuan, *et al.*

Combining laser surface texturing and double glow plasma surface chromizing to improve tribological performance of Ti6Al4V alloy[J]

Surf. Coat. Technol., 478 (2024)

Google Scholar

3. [3]

N. Lin, L. Zhang, J. Zou, *et al.*

A combined surface treatment of surface texturing-double glow plasma surface titanizing on AISI 316 stainless steel to combat surface damage: comparative appraisals of corrosion resistance and wear resistance[J]

Appl. Surf. Sci., 493 (2019), pp. 747-765

View PDFView articleView in ScopusGoogle Scholar

4. [4]

H. Yu, W. Liang, Q. Miao, *et al*.
High temperature oxidation resistance and thermodynamic properties of (TaNbZr)N and (TaNbZr)C quaternary ceramic coating[J]
Corros. Sci., 237 (2024)
Google Scholar

5. [5]

H. Zhao, Z. Ni, F. Ye
Effect of carbon content on structure and properties of WCN coatings prepared by RF magnetron sputtering[J]
Surf. Coat. Technol., 287 (2016), pp. 129-137
View PDFView articleCrossrefGoogle Scholar

6. [6]

R.K. Gupta, B. Pant, V. Kain, *et al*.
Laser shock peening and its applications: a review[J]
Lasers Manuf. Mater. Process., 6 (4) (2019), pp. 424-463
Google Scholar

7. [7]

Y. Yıldıran avcu, O. Yetik, M. Guney, *et al*.
Surface, subsurface and tribological properties of ti6al4v alloy shot peened under different parameters[J]
Materials, 13 (19) (2020), p. 4363
CrossrefGoogle Scholar

8. [8]

K. Praveenkumar, S. Swaroop, G. Manivasagam
Effect of multiple laser shock peening without coating on residual stress distribution and high temperature dry sliding wear behaviour of Ti-6Al-4V alloy[J]
Opt. Laser Technol., 164 (2023), Article 109398
View PDFView articleView in ScopusGoogle Scholar

9. [9]

S. Du, K. Zhang, Q. Meng, *et al*.
N dependent tribochemistry: achieving superhard wear-resistant low-friction TaC_xN_y films[J]
Surf. Coat. Technol., 328 (2017), pp. 378-389
View PDFView articleView in ScopusGoogle Scholar

10. [10]

V. Krasnenko, M. Brik
First-principles calculations of the structural, elastic and electronic properties of MN_xC_{1-x} (M = Ti, Zr, Hf; $0 \le x \le 1$) carbonitrides at ambient and elevated hydrostatic pressure[J]
Solid State Sci., 28 (2014), pp. 1-8
View PDFView articleView in ScopusGoogle Scholar

11. [11]

Y.H. Chang, T.L. Yoon
Effects of nitrogen addition and growth condition on the enhanced mechanical properties of transition metal carbides TMC (TM = Zr, Hf)[J]
Ceram. Int., 46 (1) (2020), pp. 1124-1136

Google Scholar

12. [12]

S. Zhang, S. Liu, D. Yan, *et al*.

Structural stability, hardness, fracture toughness and wear resistance of refractory metal carbonitrides $RMC_{1-x}N_x$ (RM = Zr, Nb, Hf, Ta) solid solutions from first-principles calculations[J]

Mater. Chem. Phys., 309 (2023)

Google Scholar

13. [13]

W. Aperador, J. Bautista-ruiz, J. Sánchez-molina

Effect of temperature on the tribological properties of hafnium carbonitrides coatings[J]

Metals, 13 (4) (2023)

Google Scholar

14. [14]

Y. Liu, Z. Tan, R. Yu, *et al*.

Anisotropic mechanical properties and electronic structures of transition metal carbonitrides M_2CN (M = V, Ti, Ta, Nb, Hf and Zr) by first-principles calculations[J]

Appl. Phys. A, 126 (2020), pp. 1-15

View PDFView articleGoogle Scholar

15. [15]

W. Li, Z. Yuan, Y. Zhu, *et al*.

Influence of nitrogen partial pressure on structure, mechanical and tribological properties of TaCN coatings[J]

Ceram. Int., 47 (18) (2021), pp. 26233-26241

View PDFView articleView in ScopusGoogle Scholar

16. [16]

W. Kao, Y. Su, H. Zhang

Mechanical and tribological properties of CrCN, CrAlN, and CrAlCN coatings deposited on tungsten carbide substrates by high-power impulse magnetron sputtering technology[J]

J. Mater. Eng. Perform. (2023), pp. 1-18

Google Scholar

17. [17]

M. Gsellmann, D. Scheiber, T. Klünsner, *et al*.

Bond strength between tin coating and microstructural constituents of a high speed steel determined by first principle calculations[J]

Acta Mater., 222 (2022)

Google Scholar

18. [18]

M. Yin, W. Liang, Q. Miao, *et al*.

Effects of plasma nitriding interlayer on adhesion and tribological behaviors of AlTiSiN coating[J]

Ind. Lubrication Tribol., 73 (6) (2021), pp. 945-953

CrossrefView in ScopusGoogle Scholar

19. [19]

M. Yin, W. Liang, Q. Miao, *et al*.

Effects of ta content on the oxidation and high-temperature tribological behaviors of (Zr, Ta) N coating

deposited by double-cathode glow plasma alloy[J]
Ceram. Int., 47 (24) (2021), pp. 34072-34085
View PDFView articleView in ScopusGoogle Scholar
20. [20]
Y. Qi, W. Liang, Q. Miao, *et al.*
Role of the nitrogen ratio on mechanical properties and wear resistance of CrN/Fe functionally graded coating produced by double glow plasma alloying[J]
Appl. Surf. Sci., 585 (2022)
Google Scholar
21. [21]
H. Yu, W. Liang, Q. Miao, *et al.*
Microstructure and wear behavior of (ZrTaNb)C/N quaternary ceramic coatings prepared by double-cathode glow plasma surface alloying on titanium alloy[J]
Wear, 523 (2023)
Google Scholar
22. [22]
N. Liu, J. Gao, L. Xu, *et al.*
Effect of carbon target current on ultralow frictional behavior of CrCN coatings under glycerol lubrication[J]
Coatings, 11 (10) (2021), p. 1155
CrossrefView in ScopusGoogle Scholar
23. [23]
N. Sala, M. Abad, J. Sánchez-lópez, *et al.*
Nb–C thin films prepared by DC-MS and HIPIMS: synthesis, structure, and tribomechanical properties[J]
Surf. Coat. Technol., 422 (2021)
Google Scholar
24. [24]
L. Rao, H. Liu, S. Liu, *et al.*
Interface relationship between TiN and Ti substrate by first-principles calculation[J]
Comput. Mater. Sci., 155 (2018), pp. 36-47
View PDFView articleView in ScopusGoogle Scholar
25. [25]
C. Chen, S. Bian, Y. Jiang, *et al.*
First principles calculations of interfacial adhesion energy between Fe substrate and transition layer of films[J]
Vacuum, 218 (2023)
Google Scholar
26. [26]
C. Sun, Y. Zheng, L. Chen, *et al.*
Thermodynamic stability and mechanical properties of (V, M)C (M = W, Mo and Cr) multicomponent carbides: a combined theoretical and experimental study[J]
J. Alloy. Compd., 895 (2022)
Google Scholar

27. [27]
S. Jiang, L. Shao, T. Fan, *et al.*
Elastic and thermodynamic properties of high entropy carbide (HfTaZrTi)C and (HfTaZrNb)C from ab initio investigation[J]
Ceram. Int., 46 (10) (2020), pp. 15104-15112
View PDFView articleView in ScopusGoogle Scholar
28. [28]
R. Akhter, Z. Zhou, Z. Xie, *et al.*
Tin versus TiSiN coatings in indentation, scratch and wear setting[J]
Appl. Surf. Sci., 563 (2021)
Google Scholar
29. [29]
M. Krbata, M. Eckert, J. Majerik, *et al.*
Wear behaviour of high strength tool steel 90MNCrV8 in contact with Si3N4[J]
Metals, 10 (6) (2020)
Google Scholar
30. [30]
A. Zaoui, B. Bouhafs, P. Ruterana
First-principles calculations on the electronic structure of TiC_xN_{1-x}, $Zr_xNb_{1-x}C$ and HfC_xN_{1-x} alloys[J]
Mater. Chem. Phys., 91 (1) (2005), pp. 108-115
View PDFView articleView in ScopusGoogle Scholar
31. [31]
J. Kim, H. Kwon, B. Kim, *et al.*
Finite temperature thermal expansion and elastic properties of (Hf1-xTax) C ultrahigh temperature ceramics[J]
Ceram. Int., 45 (8) (2019), pp. 10805-10809
View PDFView articleView in ScopusGoogle Scholar
32. [32]
Y. Zhang, S. Li, N. Li, *et al.*
Experimental and theoretical study on electronic structure and mechanical property of $Ta_xHf_{1-x}C$[J]
J. Alloy. Compd., 884 (2021)
Google Scholar
33. [33]
Y. Liu, Y. Jiang, R. Zhou, *et al.*
First principles study the stability and mechanical properties of MC (M=Ti, V, Zr, Nb, Hf and Ta) compounds[J]
J. Alloy. Compd., 582 (2014), pp. 500-504
View PDFView articleView in ScopusGoogle Scholar
34. [34]
H. Li, L. Zhang, Q. Zeng, *et al.*
Structural, elastic and electronic properties of transition metal carbides TMC (TM = Ti, Zr, Hf and Ta) from first-principles calculations[J]
Solid State Commun., 151 (8) (2011), pp. 602-606
View PDFView articleView in ScopusGoogle Scholar

35. [35]
Q. Kang, G. Wang, Q. Liu, *et al.*
Investigation for oxidation mechanism of CrN: a combination of DFT and ab initio molecular dynamics study[J]
J. Alloy. Compd., 885 (2021)
Google Scholar
36. [36]
Z. Zhang, J. Chen, G. He, *et al.*
First-principle calculations of CrN(200)/Ni(111) interface: atomic structure, stability, and electronic properties[J]
Surf. Interface Anal., 53 (2020), pp. 167-175
Google Scholar
37. [37]
Y. Liang, X. Yuan, W. Zhang
The effect of magnetostructural coupling on mechanical behaviors in CrN[J]
Solid State Commun., 150 (41) (2010), pp. 2045-2048
View PDFView articleView in ScopusGoogle Scholar
38. [38]
Y. Ren, H. Du, C. Du, *et al.*
Influence of oxygen adsorption on the chemical stability and conductivity of transition metal ceramic coatings: first-principle calculations[J]
Appl. Surf. Sci., 495 (2019)
Google Scholar
39. [39]
H. Tan, W. Si, W. Peng, *et al.*
Laser direct writing derived robust carbon nitride films with efficient photon to electron conversion for multifunctional photoelectrical applications[J]
Carbon Energy, 4 (6) (2022), pp. 1228-1241
CrossrefView in ScopusGoogle Scholar
40. [40]
H. Huang, L. Shao, H. Liu
Stacking fault energies of high-entropy nitrides from first-principles calculations[J]
Solid State Commun., 327 (2021), Article 114210
View PDFView articleView in ScopusGoogle Scholar
41. [41]
M. Yin, W. Liang, Q. Miao, *et al.*
Dependence of the m choice on the properties of Hf(M)SiCN (M = Nb, Ta, Ti, Zr) ceramic coatings: ab-initio and experimental study[J]
Tribol. Int., 196 (2024)
Google Scholar
42. [42]
J. Geng, K. An, I. Chan, *et al.*
Ab initio design of a new family of 2d materials: transition metal carbon nitrogen compounds (MCNs)[J]
J. Mater. Chem. C, 9 (14) (2021), pp. 4748-4756

CrossrefView in ScopusGoogle Scholar

43. [43]

F. Shirvani, A. Shokri, B. Ravan

Electronic, elastic and thermodynamic properties of $Ti_xZr_{1-x}N$ compounds determined via first-principles calculations[J]

Phys. B Condens. Matter, 618 (2021)

Google Scholar

44. [44]

A. Otero-de-la-roza, D. Abbasi-pérez, V. Luaña

Gibbs2: a new version of the quasiharmonic model code. II. models for solid-state thermodynamics, features and implementation[J]

Comput. Phys. Commun., 182 (10) (2011), pp. 2232-2248

View PDFView articleView in ScopusGoogle Scholar

45. [45]

H. Yu, W. Liang, Q. Miao, *et al*.

Effect of C/N incorporation on structural and crystallographic properties of TaNbZr coatings deposited by double-glow plasma surface alloying on Ti-alloy substrate[J]

Surf. Coat. Technol., 477 (2024)

Google Scholar

46. [46]

H. Yu, W. Liang, Q. Miao, *et al*.

Improvement of plasma carbonitriding modified layer on Ta15 surface by rasp-assisted DGPSA treatment[J]

Vacuum, 206 (2022)

Google Scholar

47. [47]

Y. Guo, J. Chen, W. Song, *et al*.

Electronic, mechanical and thermodynamic properties of ZrC, HfC and their solid solutions studied by first-principles calculation[J]

Solid State Commun., 338 (2021)

Google Scholar

48. [48]

W. Feng, S. Cui, H. Hu, *et al*.

Electronic structure and elastic constants of TiC_xN_{1-x}, $Zr_xNb_{1-x}C$ and HfC_xN_{1-x} alloys: a first-principles study[J]

Phys. B Condens. Matter, 406 (19) (2011), pp. 3631-3635

View PDFView articleView in ScopusGoogle Scholar

49. [49]

N. Ding, H. Jiang, C. Xu, *et al*.

Lattice distortion and the influence on mechanical and thermodynamic properties of high entropy (HfZrTaNbTi)X (X=C, N, NC) by ab initio investigation[J]

Ceram. Int., 48 (23) (2022), pp. 35353-35364

View PDFView articleView in ScopusGoogle Scholar

50. [50]

R. Akhter, Z. Zhou, Z. Xie, *et al*.
Enhancing the adhesion strength and wear resistance of nanostructured NiCrN coatings[J]
Appl. Surf. Sci., 541 (2021)
Google Scholar

51. [51]
L. Zhang, L. Chen, L. Wang
Surface modification of titanium and titanium alloys: technologies, developments, and future interests[J]
Adv. Eng. Mater., 22 (5) (2020), p. 1901258
View in ScopusGoogle Scholar

52. [52]
K. Torkashvand, A.I. Encalada, B.C.N.M. Castilho, *et al*.
High-temperature sliding wear performance of HVAF sprayed WC-based coatings with alternative binders[J]
Wear (2024), pp. 538-539
Google Scholar

53. [53]
M. Prieske, H. Hasselbruch, A. Mehner, *et al*.
Friction and wear performance of different carbon coatings for use in dry aluminium forming processes[J]
Surf. Coat. Technol., 357 (2019), pp. 1048-1059
View PDFView articleView in ScopusGoogle Scholar

54. [54]
H. Cao, H. Li, F. Liu, *et al*.
Microstructure, mechanical and tribological properties of multilayer TiAl/TiAlN coatings on Al alloys by FCVA technology[J]
Ceram. Int., 48 (4) (2022), pp. 5476-5487
View PDFView articleView in ScopusGoogle Scholar